Supporting Information for

Unlocking the Potential of Cadmium Plating Chemistry for Low-Polarization, Long-Cycling, and Ultrahigh-Efficiency Aqueous Metal Batteries

Swati Katiyar,[#a] Songyang Chang,[#a] Irfan Ullah,[a] Wentao Hou,[a] Amanda Conde-Delmoral,[a] Shen Qiu,[a] Gerardo Morell,[b] and Xianyong Wu[a]*

[a] S. Katiyar, S. Chang, I. Ullah, W. Hou, A. Condel-Delmoral, S. Qiu, and X. Wu
Department of Chemistry, University of Puerto Rico-Rio Piedras Campus, San Juan, Puerto Rico 00925-2537, United States
E-mail: xianyong.wu@upr.edu

[b]G. Morell
Department of Physics, University of Puerto Rico-Rio Piedras Campus, San Juan, Puerto Rico 00925-2537, United States

[#]These two authors contributed equally to this work.

Experimental methods

1. Materials:

The cadmium foil (99.95% purity, 0.25 mm thickness) and cadmium chloride (99.99% purity) were purchased from Sigma Aldrich. The copper foil (9 μm thickness) was the one used as current collectors for lithium-ion batteries, which was purchased from MTI corporation.

The β-phase MnO_2 material was synthesized by a hydrothermal method. Firstly, 0.25 g of polyvinyl pyrrolidone (PVP, K-30, M_W=40,000) was dissolved in 20 mL H_2O. Then 0.13 g $KMnO_4$ was dissolved in 10 mL H_2O, which was added dropwise to the PVD solution under continuous stirring. In a separate flask, 0.05 g $(NH_4)_2SO_4$ was dissolved in 10 mL H_2O, which was added dropwise to the above solution. After vigorous stirring for 15 minutes, the resulting mixture solution was transferred to a 100 mL Teflon lined stainless steel autoclave. The hydrothermal reaction was maintained at 130 °C for 10 hours. After the reaction cooled down to room temperature, the obtained precipitate was centrifuged and washed with H_2O for three times. The material was dried at 70 °C for several hours, which was further calcinated in a muffle furnace for 3 hours (target temperature: 450 °C, ramp rate: 5°C min^{-1}). The final β-MnO_2 material was in black color.

The $KNiFe(CN)_6$ material was prepared by a simple precipitation method. Typically, a solution of $NiCl_2$ (40 mL, 0.1 M) was added dropwise to the other solution of $K_3Fe(CN)_6$ (40 mL, 0.1 M) under constant stirring. After reacting for 4 hours, the dark brown precipitates were washed and centrifuged for several times, which were allowed to dry naturally in air.

2. Electrode preparations:

The MnO_2 electrode was prepared by mixing the β-phase MnO_2, Ketjen black carbon, and polyvinylidene fluoride (PVDF) binder into a homogenous slurry solution, which was later coated on carbon fiber current collectors (Fuel Cell Store, brand: AvCarb MGL370, thickness: 0.37 mm; diameter: 1.0 cm). The MnO_2 electrode was fully dried in an air-forced oven, and mass ratio between active mass, carbon, and binder is 8:1:1. The active mass loading is in the range of 1.5-2.0 mg cm^{-2}. To carry out *ex-situ* XRD analysis, we prepared the MnO_2 self-standing film electrode, which comprises 70 wt.% MnO_2, 20 wt.% Ketjen carbon, and 10 wt.% polytetrafluoroethylene (PTFE) binder. The $KNiFe(CN)_6$ electrode consists of 70 wt.% active material, 20 wt.% Ketjen black carbon, and 10 wt.% PVDF binder, where the active mass loading is ~1.5 mg cm^{-2}.

The cadmium foil was cut into round-shape electrodes for use in symmetrical Cd‖Cd and asymmetrical Cd‖Cu batteries, whose area is 0.71 cm^2 (diameter: 3/8 inches). The area for Cd foil is 1.27 cm^2 (diameter: 1/2 inches) in Cd‖MnO_2 batteries.

3. Battery assembly and testing:

The symmetrical Cd‖Cd batteries (2032 type coin cells) were made by sandwiching two Cd foils by glass fiber separators. The asymmetrical Cd‖Cu batteries (2032 type coin cells) were made by using the Cd foil as the counter/reference electrodes and copper foils as the working electrodes. The electrolyte is ~100 μL $CdCl_2$ aqueous solution. The Cd‖MnO_2 batteries were made in the two-electrode Swagelok cell configuration, where the working electrode is MnO_2, and the counter/reference electrode is the Cd foil. To observe the *ex-situ* SEM images or the *ex-situ* XRD patterns, the Cd or MnO_2 electrodes were retrieved carefully from the cycled batteries, and these electrodes were washed by water and isopropanol multiple times. The $KNiFe(CN)_6$‖Cd hybrid batteries were also made in the two-electrode Swagelok cell configuration, where the electrolyte was 1.0 M $CdCl_2$ + 1.0 M KCl.

Due to the toxicity of Cd metal and salts, cautions and necessary personal protective equipment (lab coats, gloves, and face masks) are needed when handling these chemicals. The waste $CdCl_2$ electrolyte, the waste Cd metals, and Cd coin cells were collected and stored in specific vials or containers, which were processed by the EHS personnels.

To analyze the cyclic voltammetry curve of the electrolyte, we assembled three-electrode Swagelok cells, where the working, counter, and reference electrode is a titanium foil, a Cd foil, and silver/silver chloride electrode (Ag/AgCl, saturated, +0.20 V *vs.* SHE), respectively. The linear scanning voltammetry of the 0.1 M NH_4Cl solution was made in a three-electrode breaker cell configuration, where the Cd foil, a large piece of activated carbon, and Ag/AgCl served as the working, counter, and reference electrode, respectively.

To further confirm the K^+ insertion in the hybrid battery, we also made two more batteries for comparison. The Cd-$KNiFe(CN)_6$ battery was made in the two-electrode Swagelok cell, with Cd metal as the anode, $KNiFe(CN)_6$ as the cathode, and 1 M $CdCl_2$ solution as the electrolyte. We also tested the pure K^+ insertion performance in the $KNiFe(CN)_6$ material, where the $KNiFe(CN)_6$ is the working electrode, a large piece of activated carbon self-standing film is the counter electrode, 1 M KCl is the electrolyte, and saturated Ag/AgCl electrode is the reference electrode.

To test the corrosion curve of the Cd metal in the 1 M CdCl electrolyte, we assembled symmetrical Cd batteries in the 2032 coin cell, where the area of Cd metal is 0.71 cm^2.

Galvanostatic charge/discharge curves were obtained on the Landt battery cycler (CT3002AU). The Cd plating efficiency in each GCD cycle was calculated through dividing the stripping (charge) capacity by plating (discharge) capacity, namely CE% = stripping/plating * 100%. The average plating efficiency was calculated by adding all these efficiencies together,

and then dividing them by the total cycle numbers, namely average CE% = 1/n * $\sum(CE_1 + CE_2 + CE_3\ldots + CE_n)$. Cyclic voltammetry, linear scanning voltammetry, corrosion curves, and electrochemical impedance spectra results were tested on a Biologic SP-150 Potentiostat.

4. Physical characterization:

X-ray diffraction (XRD) patterns of the MnO_2 powders and self-standing film electrodes were collected on the Rigaku SuperNova equipped with a HyPix3000 X-ray detector and CuKα radiation source (λ = 1.5406 Å). Scanning electron microscopy (SEM) images and energy dispersive X-ray spectra (EDS) mapping of MnO_2 and cadmium foils were recorded at a field emission scanning electron microscope (SEM, JEOL, JSM-6480LV).

5. Calculation of the Cd-MnO_2 battery energy density

If the N/P ratio is 1:1, the average capacity can be calculated as C1*C2/(C1+C2) = 310*477/(310+477) = 188 mAh g^{-1}. The battery voltage is 1.0 V. Therefore, the theoretical energy density is calculated as 188*1 = 188 Wh kg^{-1} (based on the cathode and anode active mass).

If the N/P ratio is 2:1, the capacity of the Cd metal will be 477/2 = 238.5 mAh g^{-1}. The average capacity will be 310*238.5/(310+238.5) = 135 mAh g^{-1}. The theoretical energy density is 135*1 = 135 Wh kg^{-1} (based on the cathode and anode active mass). If we further assume 40-50 wt.% mass burden is from non-active components, including the current collectors, electrolytes, carbon, binders, and packages, the final energy density will be 135 * (50-60%) = 67-80 Wh kg^{-1}.

Table S1. The comparison of divalent metal elements in terms of the molar mass, standard electrode potential, gravimetric capacity, volumetric capacity, density, and elemental price.

Elements	Molar mass / g mol^{-1}	Standard electrode potential of M^{2+}/M / V *vs.* SHE	Gravimetric capacity / mAh g^{-1}	Volumetric capacity / mAh cm^{-3}	Metal density / g cm^{-3}	Elemental price / USD kg^{-1}
Mn	54.94	-1.18	976	7036	7.21	1.82
Fe	55.85	-0.44	960	7559	7.87	0.424
Ni	58.69	-0.26	913	8133	8.91	13.9
Cu	63.55	+0.34	844	7562	8.96	6.0
Zn	65.38	-0.76	820	5846	7.14	2.55
Sn	118.7	-0.13	452	3280	7.265	18.7
Cd	112.4	-0.40	477	4125	8.65	2.73

Note that the theoretical gravimetric capacity is calculated based on the equation of C = nF/3.6M, where C, n, F, and M represents the theoretical capacity, electron transfer number (n=2), Faraday constant (96485 C/mol), and molar mass, respectively. The volumetric capacity is calculated by multiplying the gravimetrical capacity with the metal density. The elemental price information is retrieved from the Wikipedia page.[1]

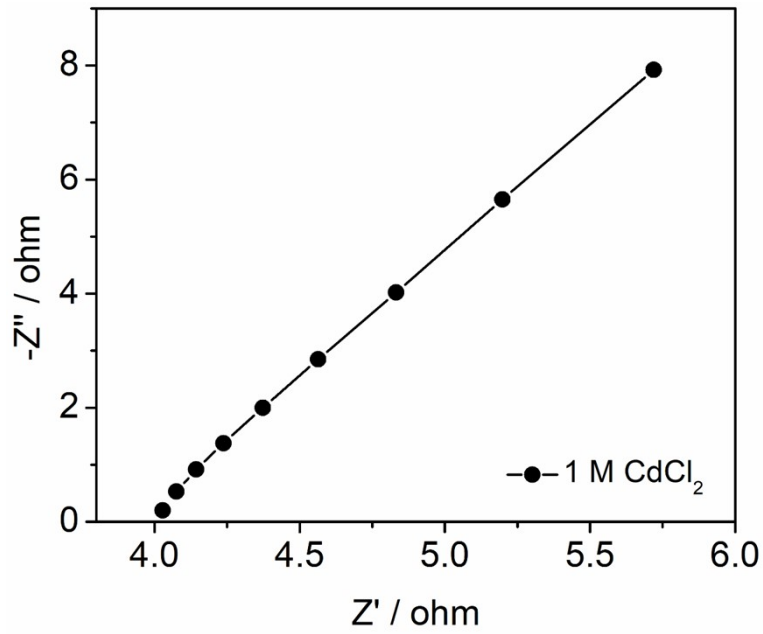

Figure S1. The electrochemical impedance spectra (EIS) result of the 1.0 M $CdCl_2$ electrolyte. We calculated the electrolyte ionic conductivity as ~20.8 mS cm^{-1} based on the equation of $\sigma=1/\rho=L/(R\cdot S)$, where L, R, and S represents the distance, the resistance, and surface area, respectively. In this case, the electrolyte resistance (R) is 4.01 Ω, the titanium electrode area (S) is 1.27 cm^2, and the distance (L) between two titanium electrodes is 0.106 cm.

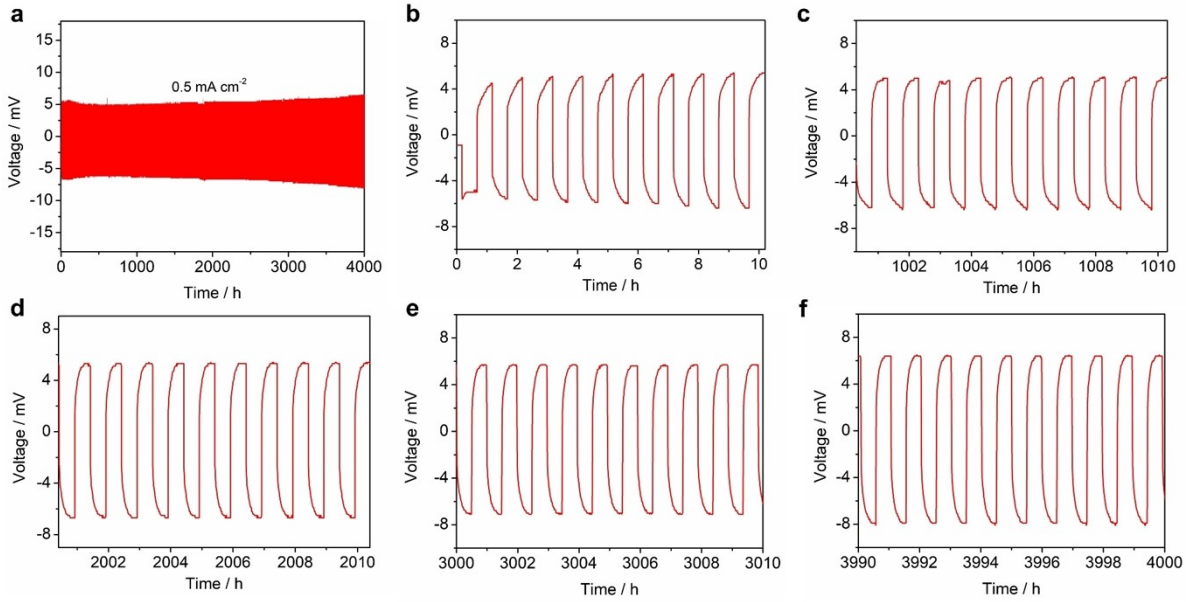

Figure S2. The symmetrical Cd‖Cd battery performance at 0.5 mA cm^{-2} and 0.25 mAh cm^{-2}. Each charge or discharge process is 30 minutes. (a) The overall GCD curves; (b-f) Selected GCD curves at different testing cycles.

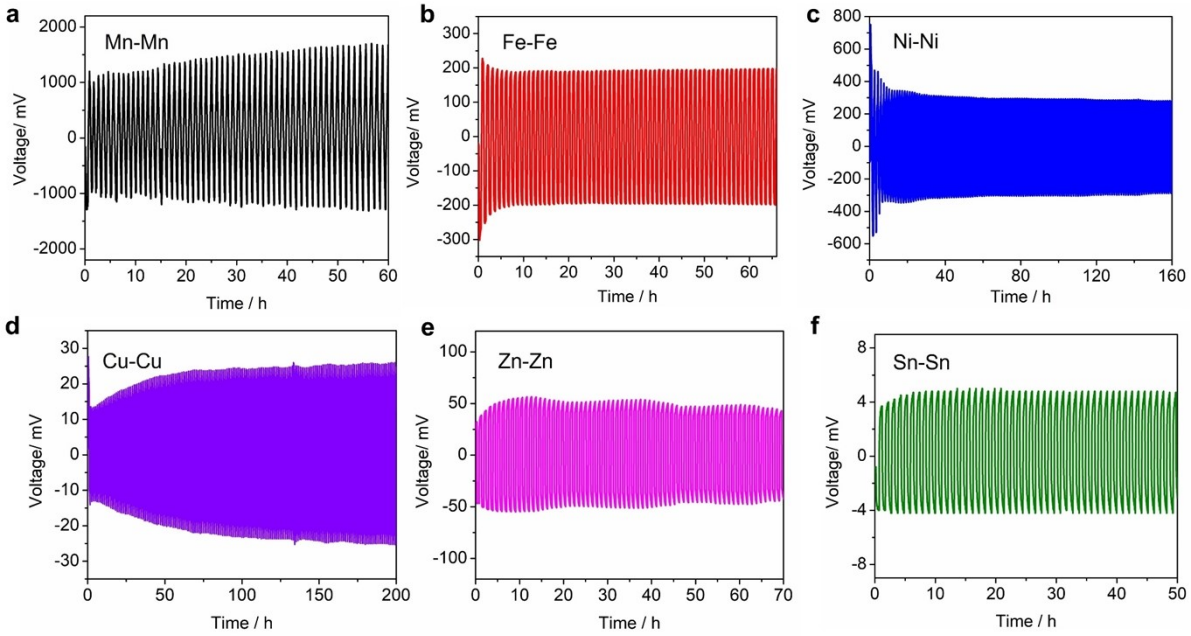

Figure S3. The GCD curves of other symmetrical divalent M||M batteries, where M = Mn, Fe, Ni, Cu, Zn, and Sn (a-f). The testing condition is identical to the Cd||Cd battery (0.5 mA cm^{-2} current density and 0.25 mAh cm^{-2} capacity). Reprinted with permission from *J. Am. Chem. Soc. 2023, 145, 45, 24746-24754*. Copyright, 2023, American Chemical Society.

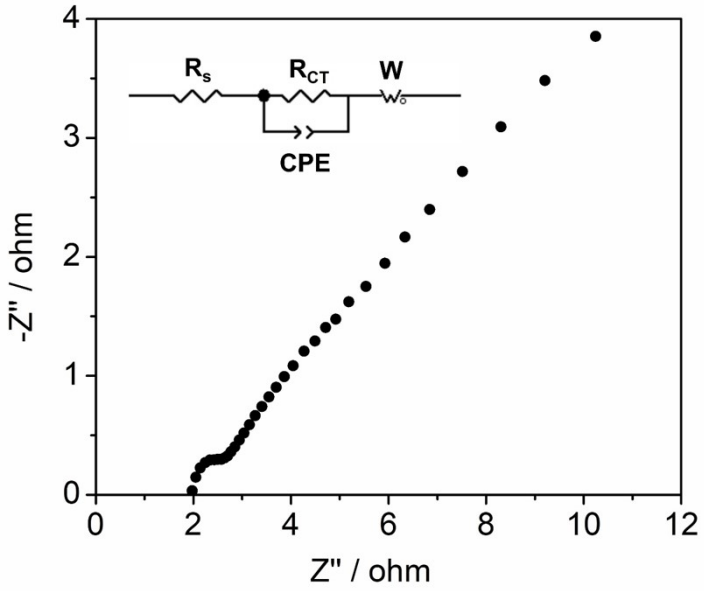

Figure S4. The EIS result of the symmetrical Cd||Cd battery at room temperature. The equivalent circuit diagram is provided in the figure inset. As shown, the charge-transfer resistance (R_{CT}) is fitted as ~0.29 ohm, which is quite small. Therefore, the Cd^{2+}/Cd redox exhibits fast reaction kinetics, leading to the small polarization in the symmetrical Cd||Cd batteries.

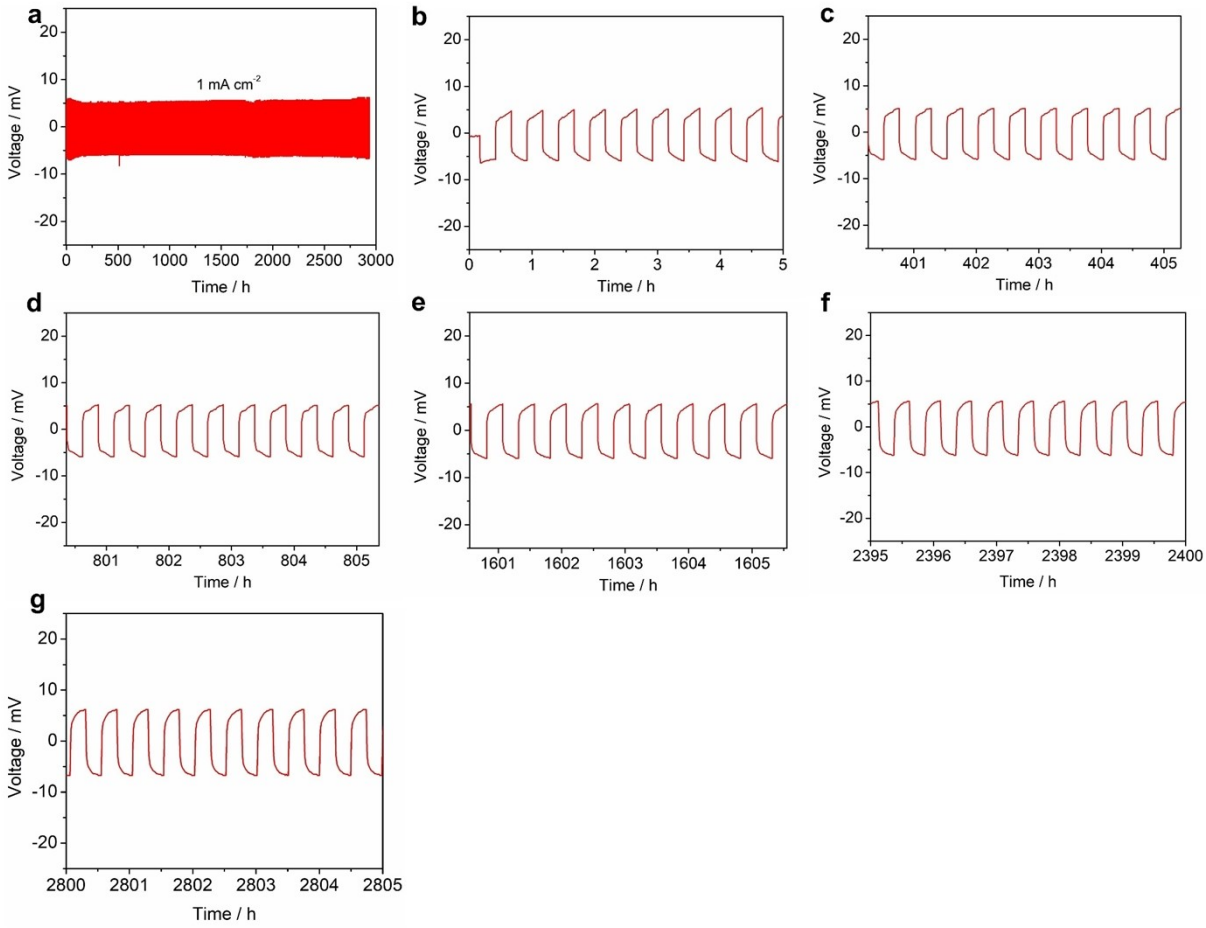

Figure S5. The symmetrical Cd||Cd battery performance at 1.0 mA cm^{-2} current density and 0.25 mAh cm^{-2}. Each charge or discharge process is 15 minutes. (a) The overall GCD curves; (b-g) The selected GCD curves at different testing cycles.

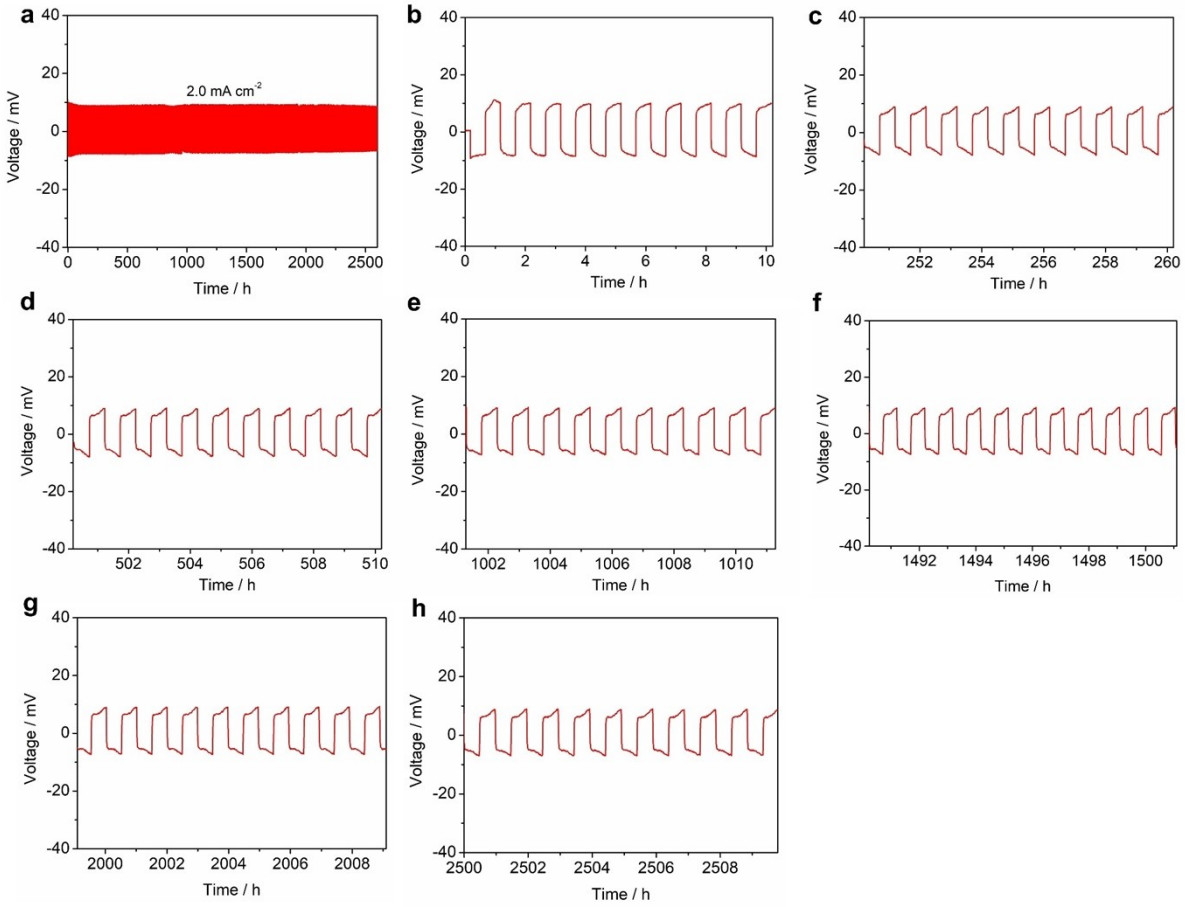

Figure S6. The symmetrical Cd||Cd battery performance at 2.0 mA cm^{-2} current density and 1.0 mAh cm^{-2}. Each charge or discharge process is 30 minutes. (a) The overall GCD curves; (b-h) The selected GCD curves at different testing cycles.

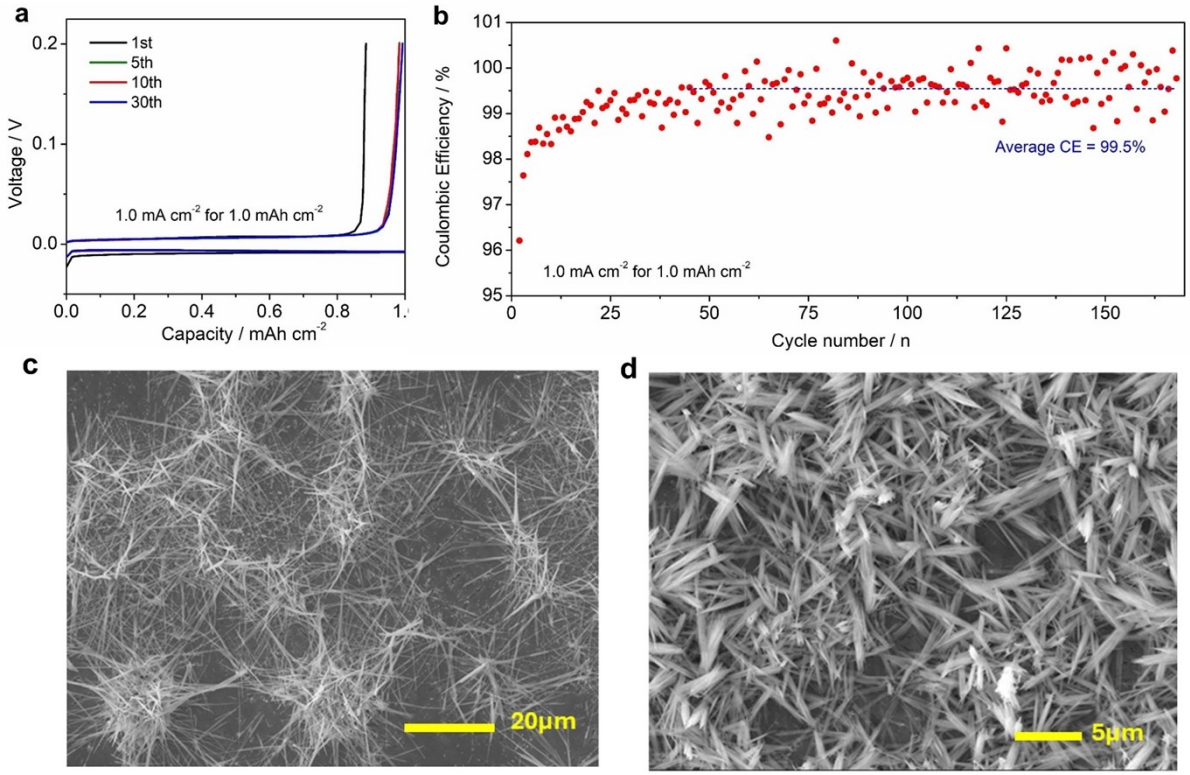

Figure S7. The Cd plating performance using a Ti foil current collector. (a) The GCD curves of Cd‖Ti batteries; (b) The cycling performance at 1.0 cm^{-2} and 1.0 mAh cm^{-2}; (c) The SEM image of plated Cd metals at 0.5 mAh cm^{-2} capacity; (d) The SEM image of plated Cd metals at 1.0 mAh cm^{-2} capacity.

As shown, the plated Cd on the Ti foil appears as dendrite-like whiskers, which are much inferior to the plate-like morphology on the Cu foil. The large surface area will exert more side reactions with electrolytes, leading to the lower Cd plating efficiency on the Ti foil. Besides, these dendrites will cause micro or soft battery short-circuits, which explain the more fluctuation in the Cd||Ti plating efficiency.

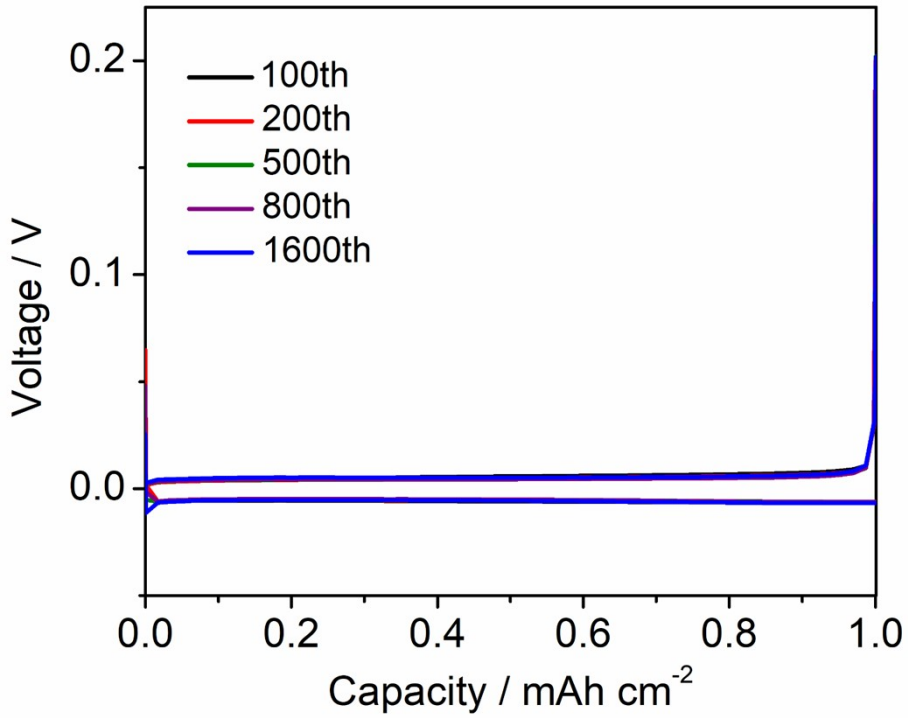

Figure S8. The selected GCD curve of Cd||Cu batteries at different cycles.

Table S2. The performance comparison between our Cd metal anode and some representative Zn metal batteries.

Approaches	Anode	Electrolyte	Current density (mA cm^{-2})	Areal capacity (mAh cm^{-2})	CE	Cycle number	Cycle time	Source
High concentration electrolytes	Zn	20 m LiTFSI + 1 m $Zn(TFSI)_2$	1	0.71	99.7%	200	284 h	[2]
	Zn	30 m $ZnCl_2$ + 5 m LiCl	1	4	99.7%	100	800 h	[3]
	Zn	30 m $ZnCl_2$ + 10 m TMACl + 5 m LiCl in H_2O/DMC	0.2	6.5	99.95%	50	300 h	[4]
	Zn	4 m $Zn(OTF)_2$ + 0.5 m Me_3EtNOT + H_2O	0.5	0.5	99.8%	1000	2000 h	[5]
	Zn	7.6 m $ZnCl_2$ + 0.05 m $SnCl_2$	1	0.5	99.7	200	200 h	[6]
Additives	Zn	2 M $ZnSO_4$ +0.0085 M $La(NO_3)_3$	2	1	99.9%	2100	2100 h	[7]
	Zn	2 M $ZnSO_4$ H_2O/methane	1	0.5	99.7%	900	900 h	[8]
	Zn	1 m $ZnSO_4$ + 10% acetonitrile	1	1	99.61%	500	1000 h	[9]
	Zn	2 M $ZnSO_4$ + 1.5 mM Rb_2SO_4	0.5	0.25	99.16%	500	500 h	[10]
	Zn	2 M $ZnSO_4$ + 0.05 mM TBA_2SO_4	10	10	98%	200	400 h	[11]
Anode modification	Zn@IS	2 M $ZnSO_4$	2	1	99.16%	200	200 h	[12]
	Zn@ZnO	2 M $ZnSO_4$	2	0.5	99.55%	300	150 h	[13]
	Zn@ZIF-8	2 M $ZnSO_4$	2	1	98.6%	200	200 h	[14]
	Zn/In	1 M $ZnSO_4$	1	1	98.88%	200	400 h	[15]
	Zn@IHS	1 M $ZnSO_4$	5	0.5	99.6%	50	10 h	[16]
1 M electrolyte, no additives or modification	**Cd**	**1 M $CdCl_2$**	**1**	**1**	**99.92%**	**1622**	**3243 h**	**This work**

Note that some studies were not ploted in the main context figure, because of their relatively low efficiencies and short plating time.

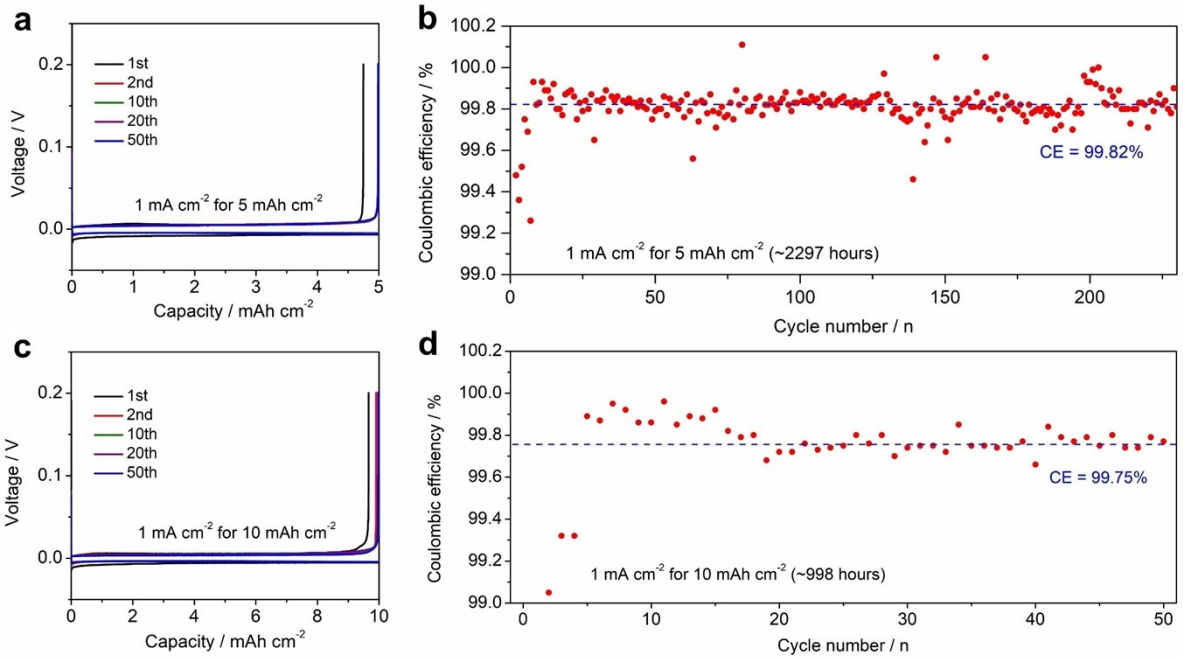

Figure S9. The plating performance of Cd‖Cu batteries with higher capacities. (a-b) GCD curves and cycling performance at 1 mA cm^{-2} current and 5 mAh cm^{-2} capacity; (c-d) GCD curves and cycling performance at 1 mA cm^{-2} current and 10 mAh cm^{-2} capacity.

Note that we intentionally plot the efficiencies in a very narrow range of 99-100.2%, so that readers can clearly see detailed values. These efficiencies appear to be "fluctuating", but most of them are very close to each other (less than ±0.20% difference), indicating a stable plating/stripping process.

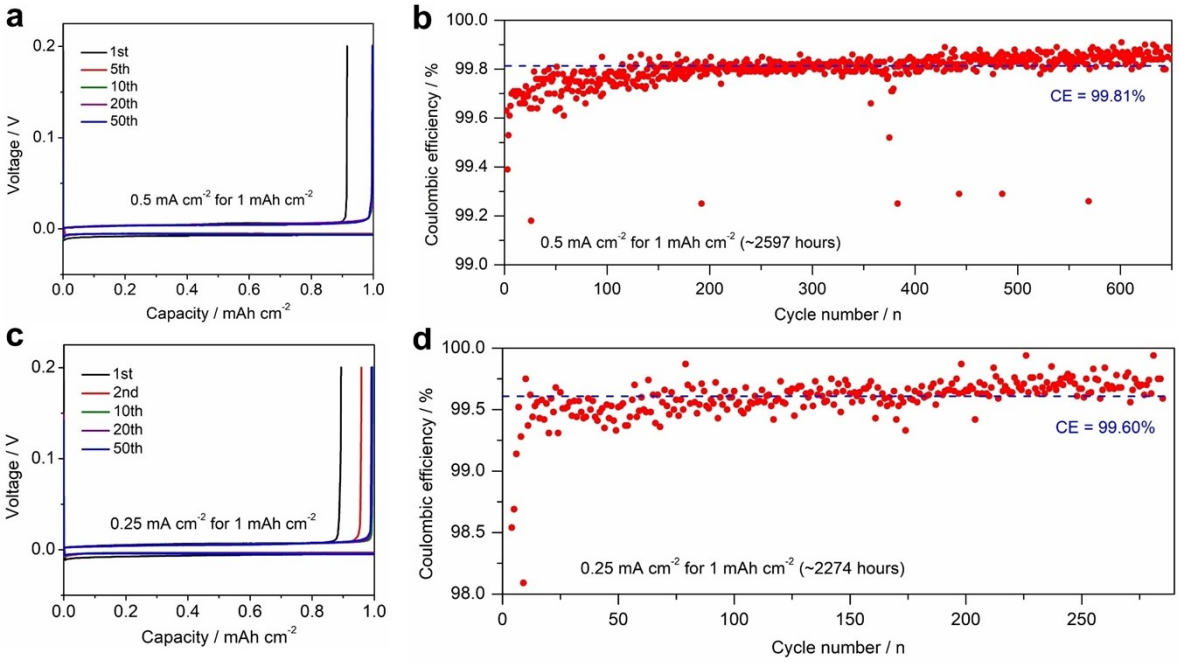

Figure S10. The plating performance of Cd‖Cu batteries with low current densities. (a-b) GCD curves and cycling performance at 0.5 mA cm^{-2} current and 1 mAh cm^{-2} capacity; (c-d) GCD curves and cycling performance at 0.25 mA cm^{-2} current and 1 mAh cm^{-2} capacity.

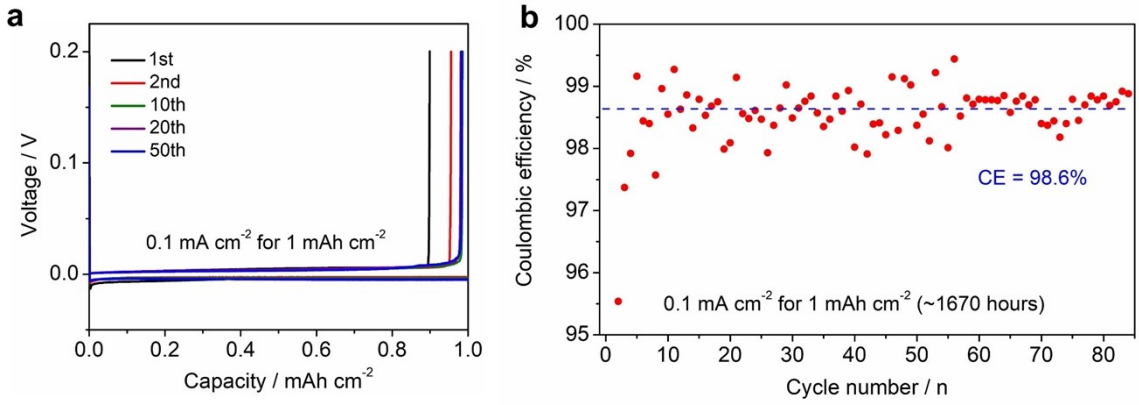

Figure S11. The plating performance of the Cd‖Cu battery at a small current density of 0.1 mA cm^{-2}. (a) The selected GCD curves; (b) The Coulombic efficiency during the cycling. Due to the initial activation process, the average CE was calculated from the 6^{th} to 84^{th} cycle.

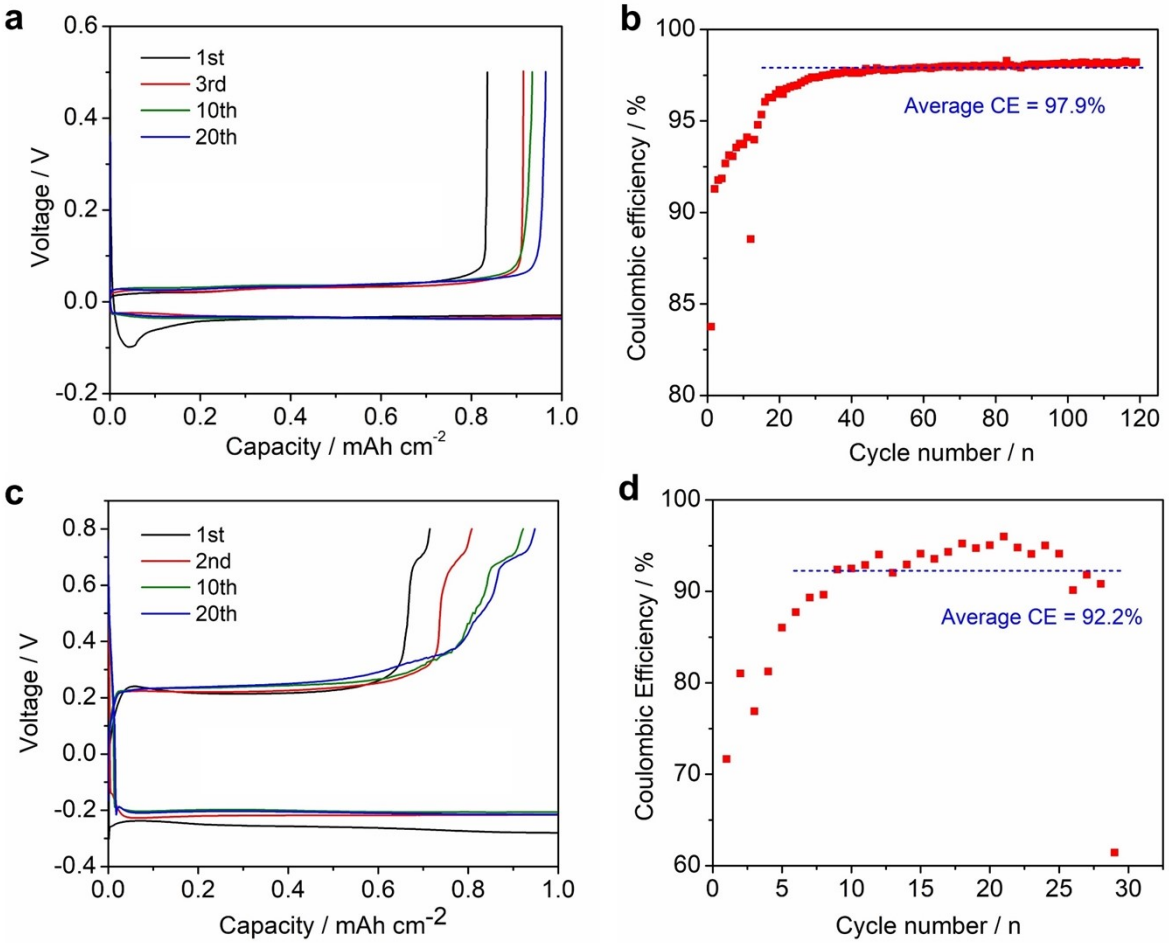

Figure S12. (a-b) The plating performance of Zn‖Cu batteries; (c-d) The plating performance of Fe‖Ti batteries. These batteries were tested at identical conditions to Cd‖Cu batteries, where the current density is 0.25 mA cm^{-2}, and the area capacity is 1.0 mAh cm^{-2}.

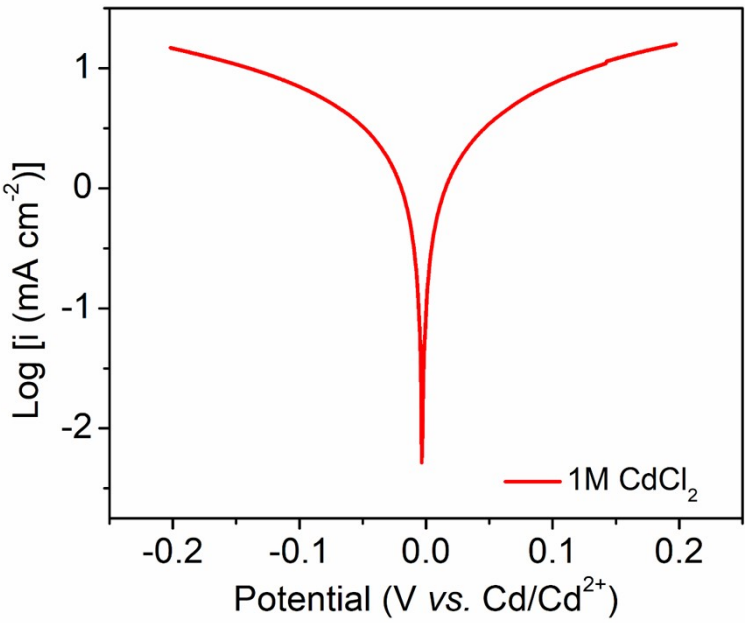

Figure S13. The corrosion curve of the Cd metal in the 1 M $CdCl_2$ electrolyte.

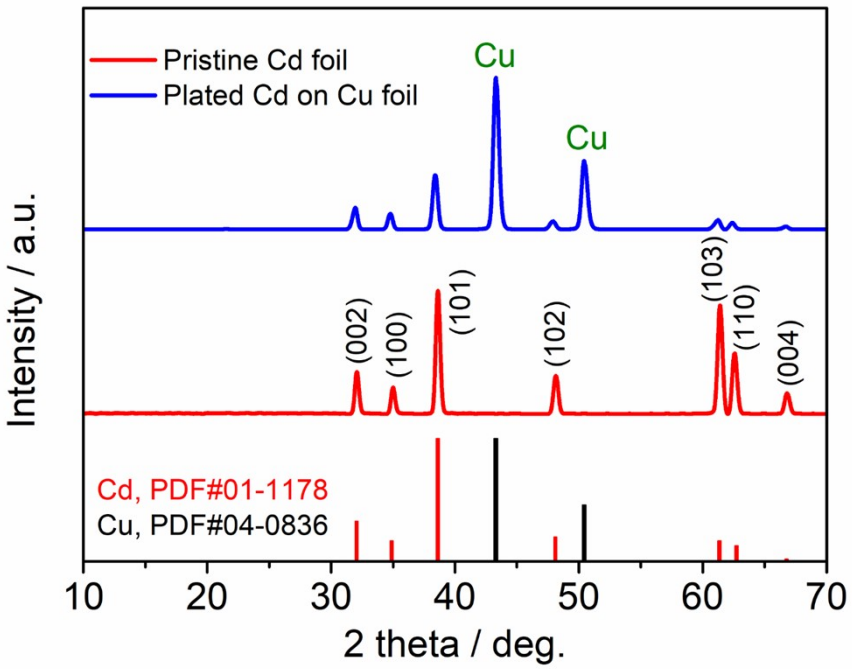

Figure S14. XRD patterns of the plated Cd metal on the copper foil with a comparison of the pristine Cd foil.

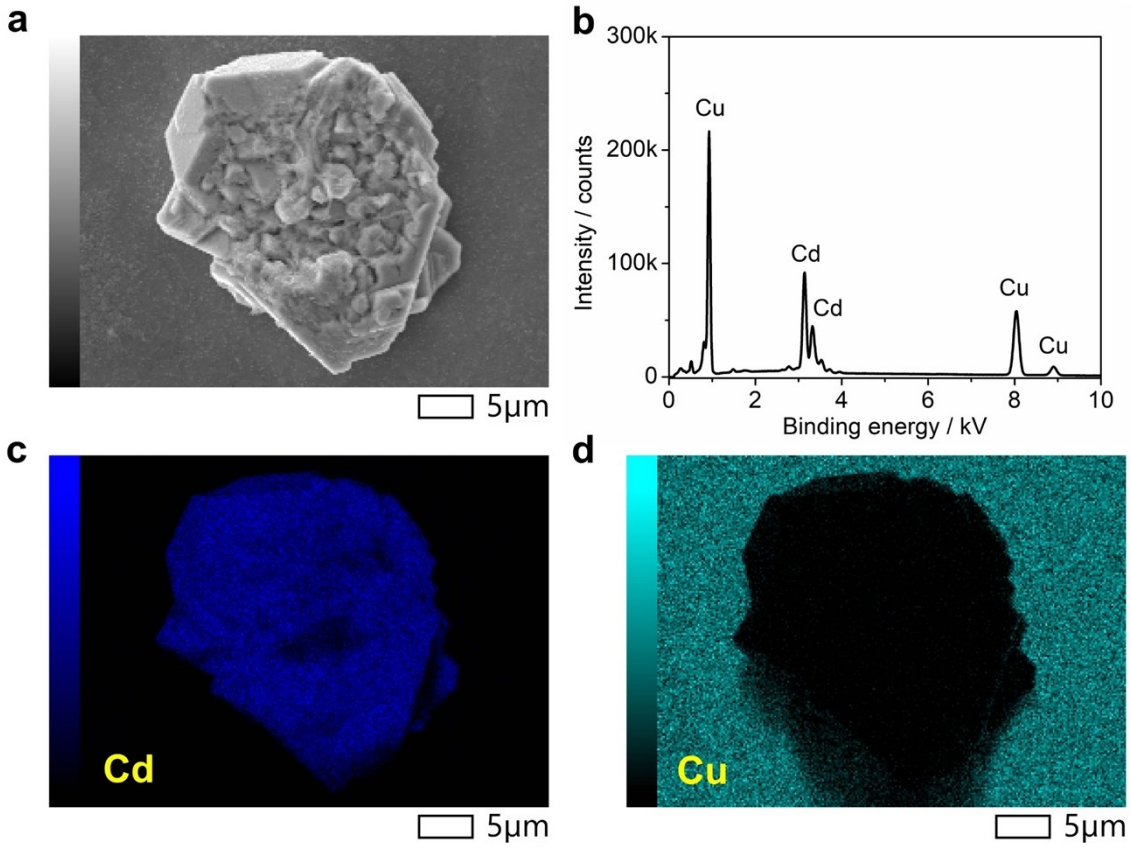

Figure S15. The EDS mapping of the plated Cd metal at 1.0 mA cm^{-2} and 1.0 mAh cm^{-2}. (a) The SEM image; (b) The EDS result; (c-d) The EDS mapping results of the Cd metal on the Cu foil current collector.

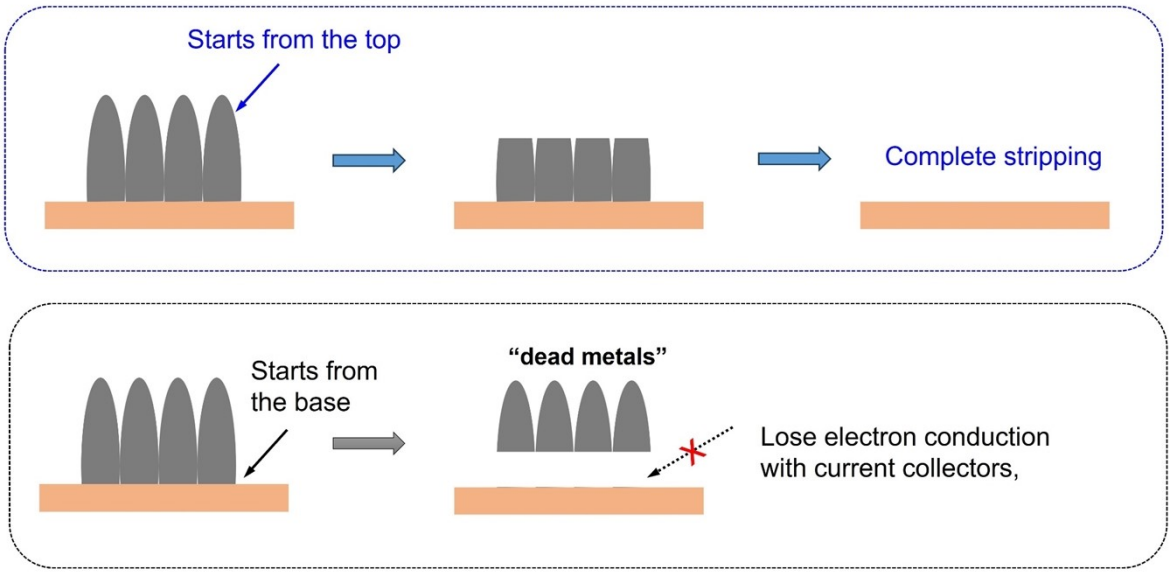

Figure S16. The schematic to show the difference between the top stripping and base stripping.

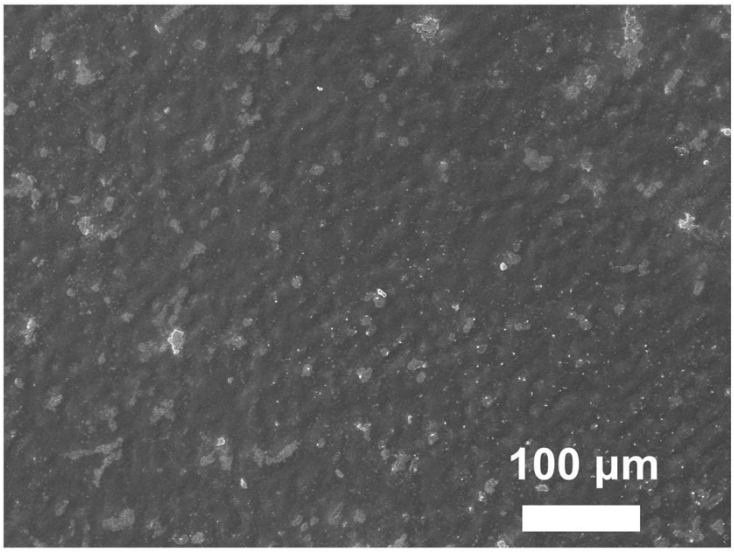

Figure S17. The SEM image of the stripped electrode at 0.2 V (point D).

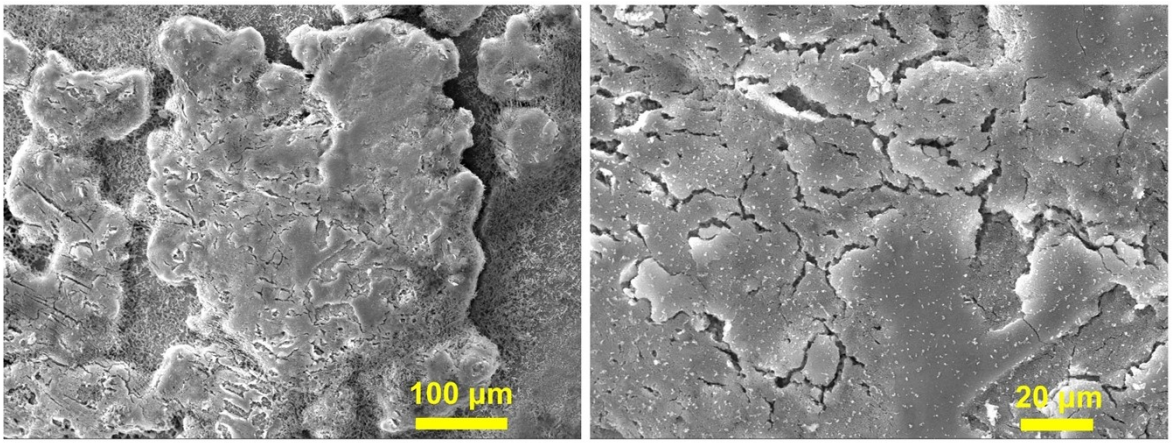

Figure S18. The SEM images of the Cd metal at a high plating capacity of 5.0 mAh cm^{-2}. The current density is 1.0 mA cm^{-2}.

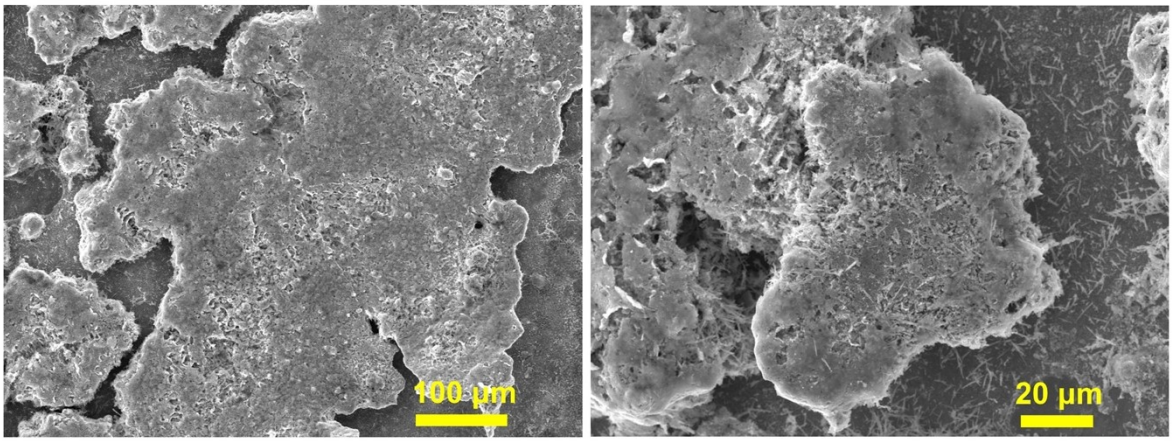

Figure S19. The SEM images of the Cd metal at a high plating capacity of 10.0 mAh cm^{-2}. The current density is 1.0 mA cm^{-2}.

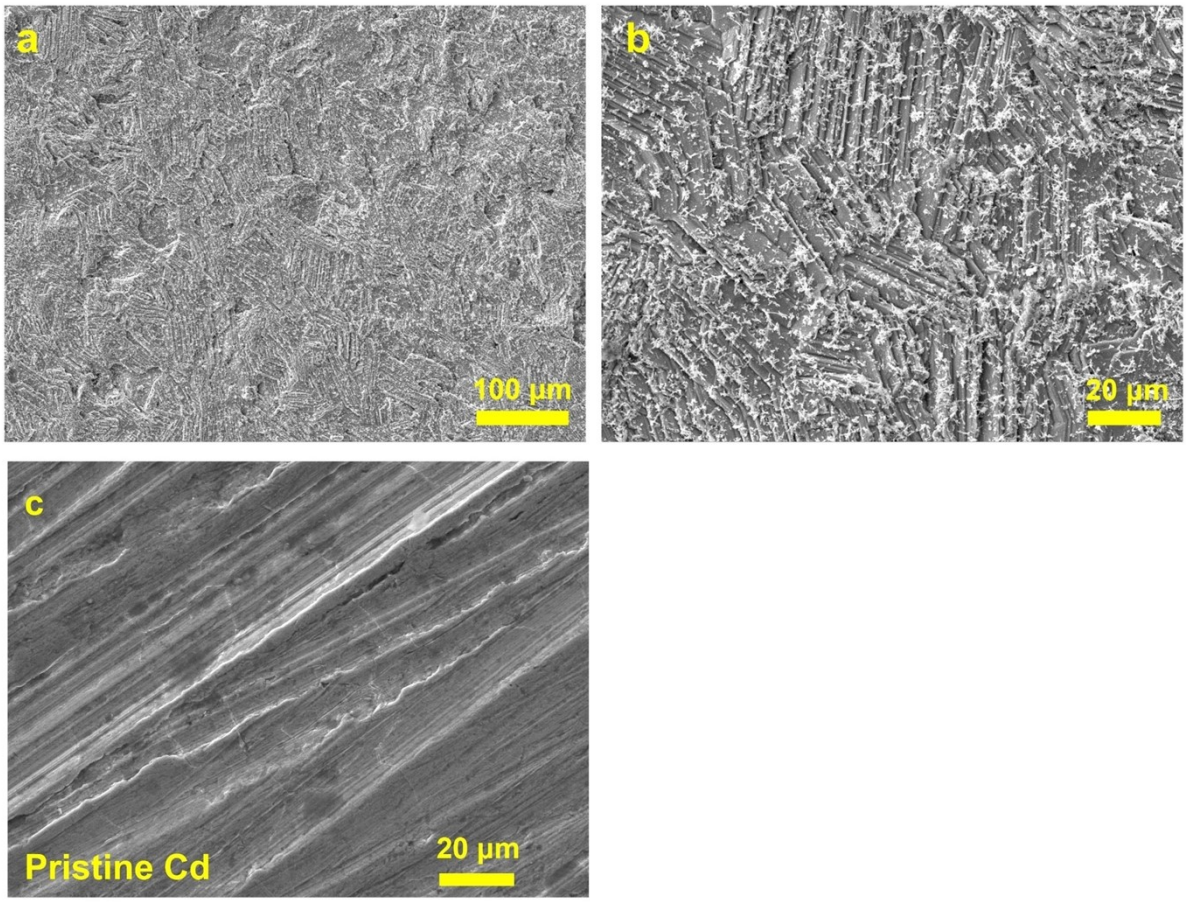

Figure S20. (a-b) The Cd metal morphology after cycling for 200 hours in symmetrical batteries, where the testing condition is 1.0 mA cm^{-2} for 0.5 mAh cm^{-2}; (c) The SEM image of the pristine Cd foil.

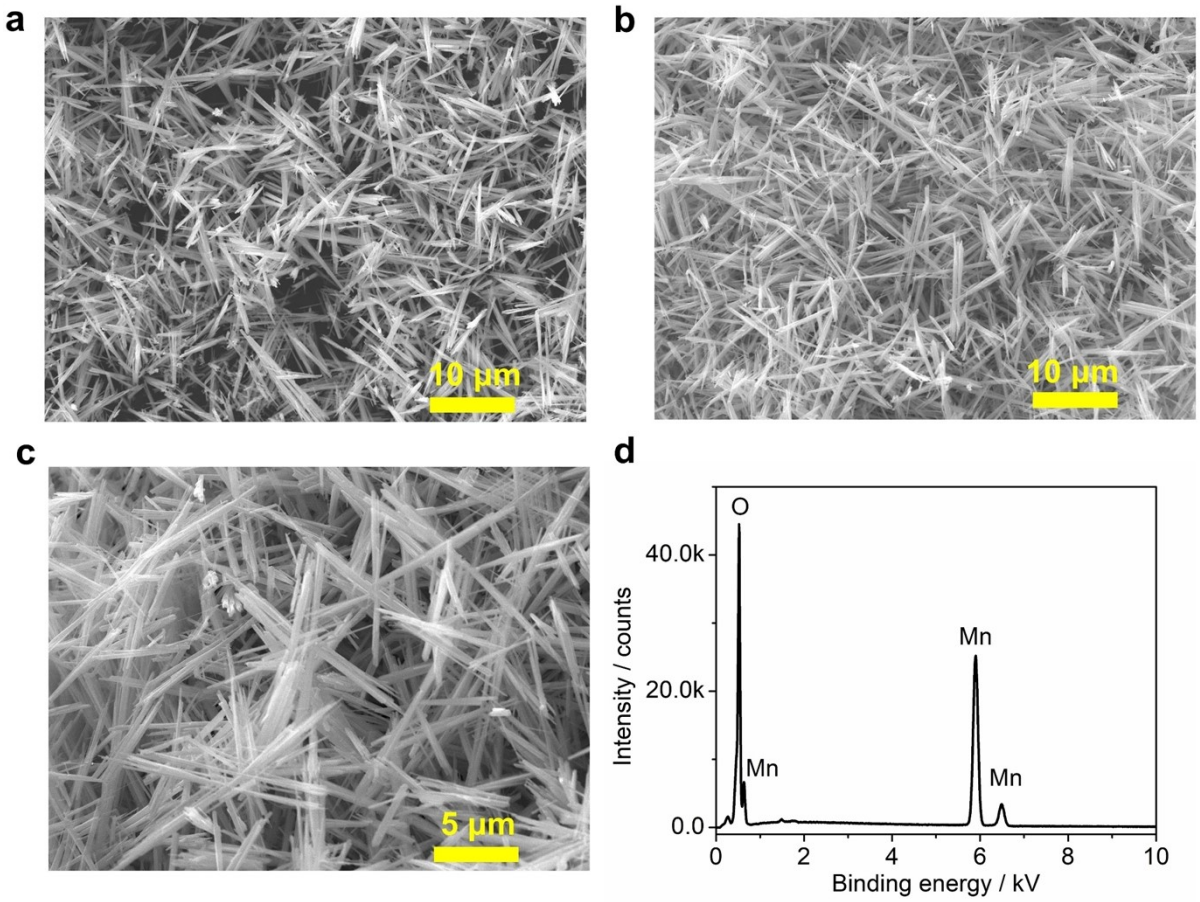

Figure S21. (a-c) The SEM images of MnO_2; (d) The EDS result, where only Mn and O elements are present, which confirms the chemical purity.

Table S3. The comparison between the Cd-MnO_2 battery with representative metal batteries in terms of capacity, voltage, and energy density.

Citation	Battery system	Cathode capacity / mAh g^{-1}	Anode capacity / mAh g^{-1}	Cell voltage / V	Energy density / Wh kg^{-1}
[17]	Fe-I_2	190	~960	0.91	~144
[18]	Fe-S	~1050	~960	0.4	~200
[19]	Zn-$FeFe(CN)_6$	~78	~820	1.5	106
[20]	Zn-$Zn_3[Fe(CN)_6]_2$	~65.4	~820	1.7	100
[21]	Zn-MnO_2	240	~820	~1.3	241
[22]	Zn-MnO_2	285	~820	~1.44	~304
[23]	Zn-V_2O_5	381	~820	0.7	144
[24]	Zn- $Zn_{0.25}V_2O_5$	270	~820	0.8	162
[25]	Zn-VO_2	353	~820	0.6	148
This work	Cd-MnO_2	310	477	~1.0	188

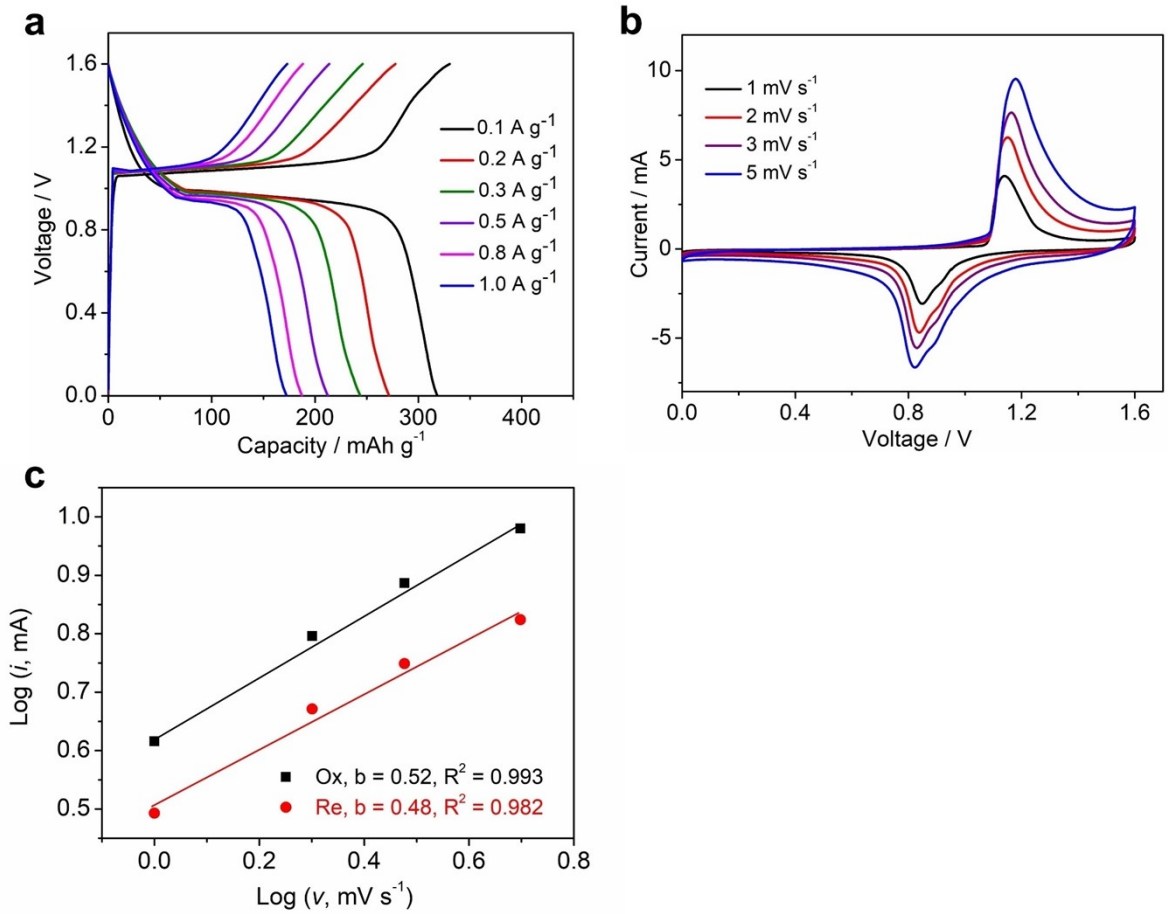

Figure S22. (a) The rate performance; (b) CV curves at different scanning rates; (c) The linear fitting of the *b* value for oxidization and reduction peaks.

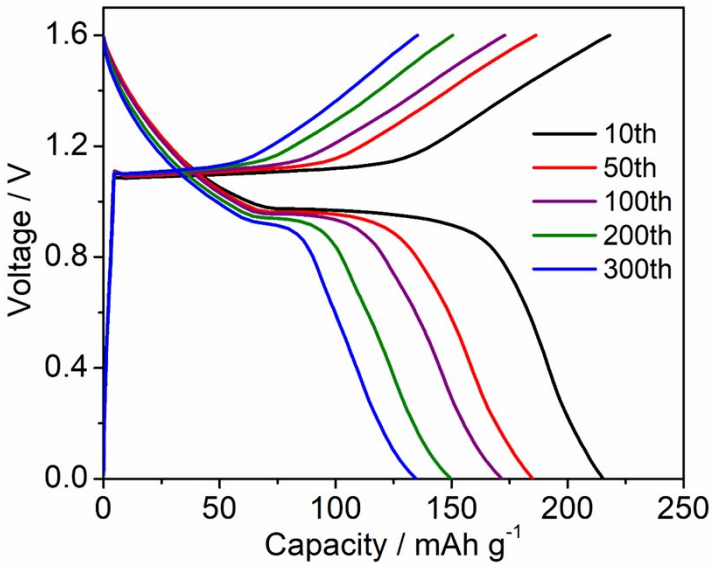

Figure S23. The selected GCD curves of the Cd-MnO_2 battery during cycling.

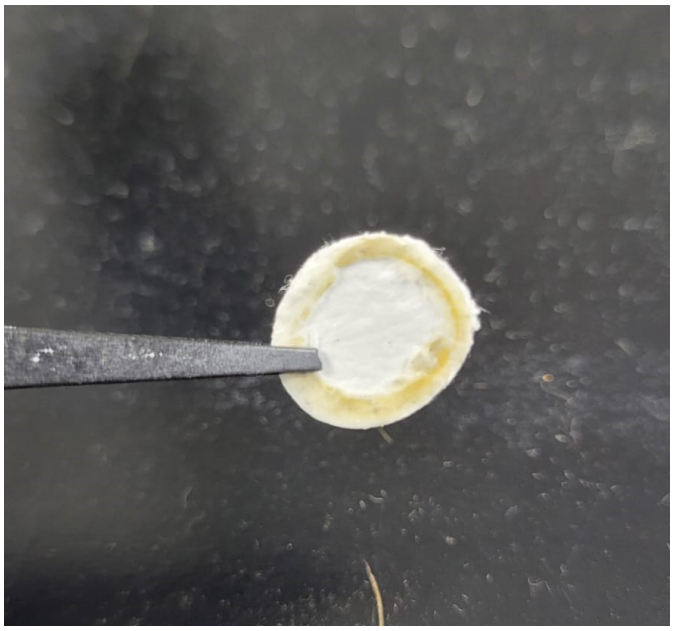

Figure S24. The photo of the separator that was retrieved from the Cd-MnO_2 battery after cycling.

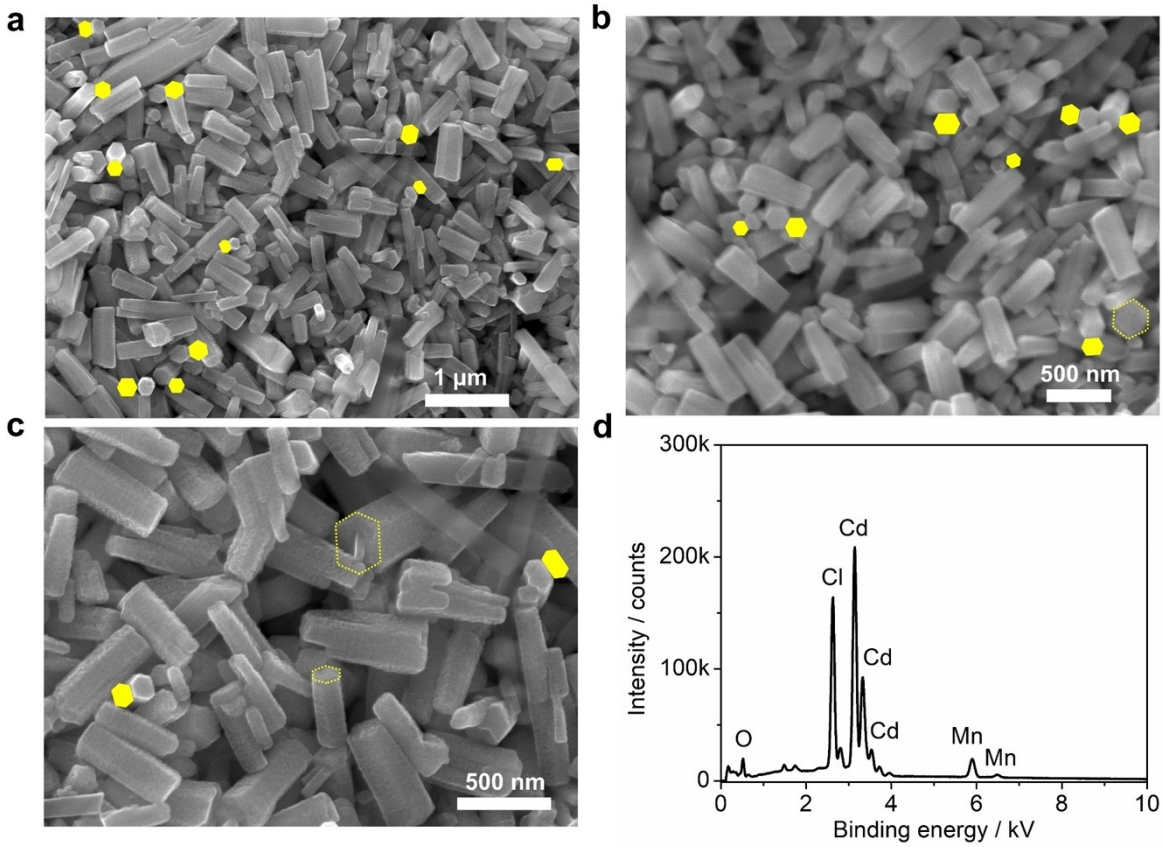

Figure S25. (a-c) SEM images of the MnO_2 electrode at the initial discharge state (point B); (d) The EDS result of the MnO_2 electrode.

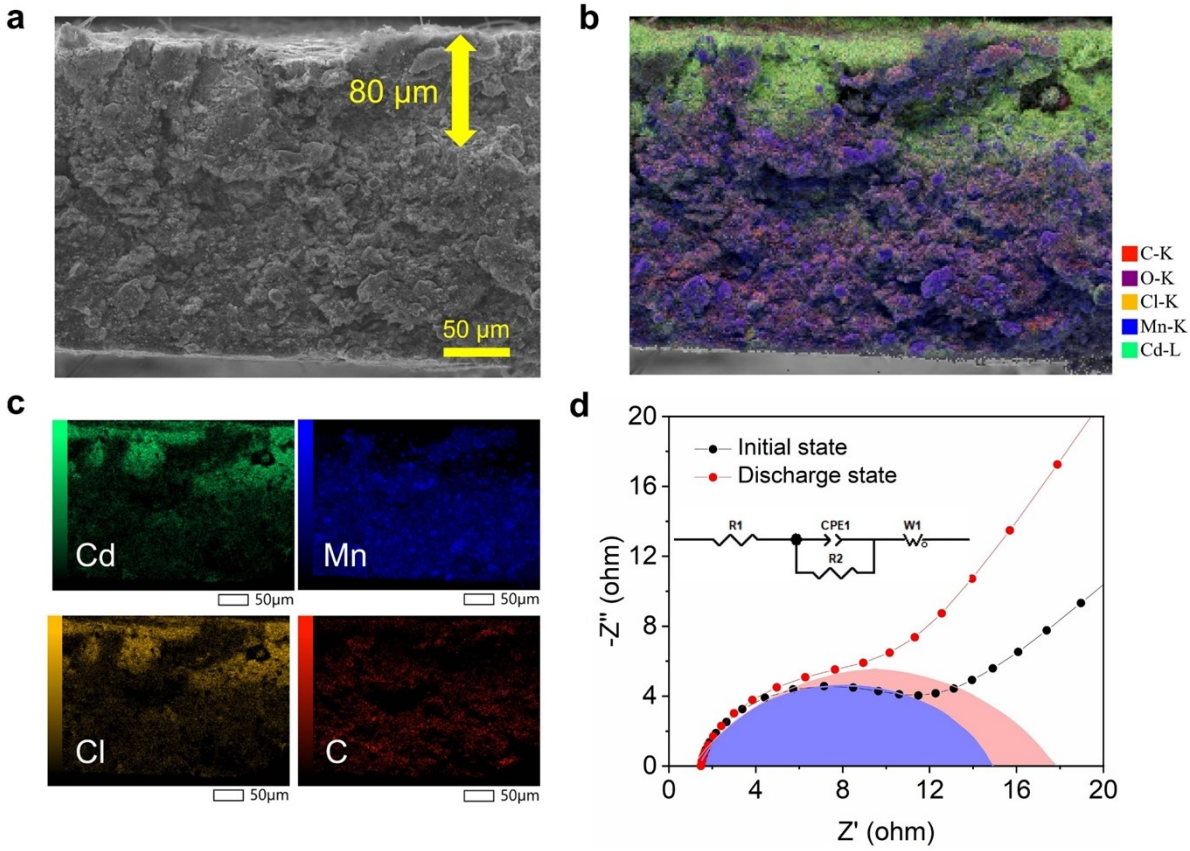

Figure S26. (a-c) Cross-sectional morphology and mapping analysis of the MnO_2 electrode after discharge. (d) Electrochemical impedance spectrum (EIS) of the Cd-MnO_2 battery at the pristine and discharged states.

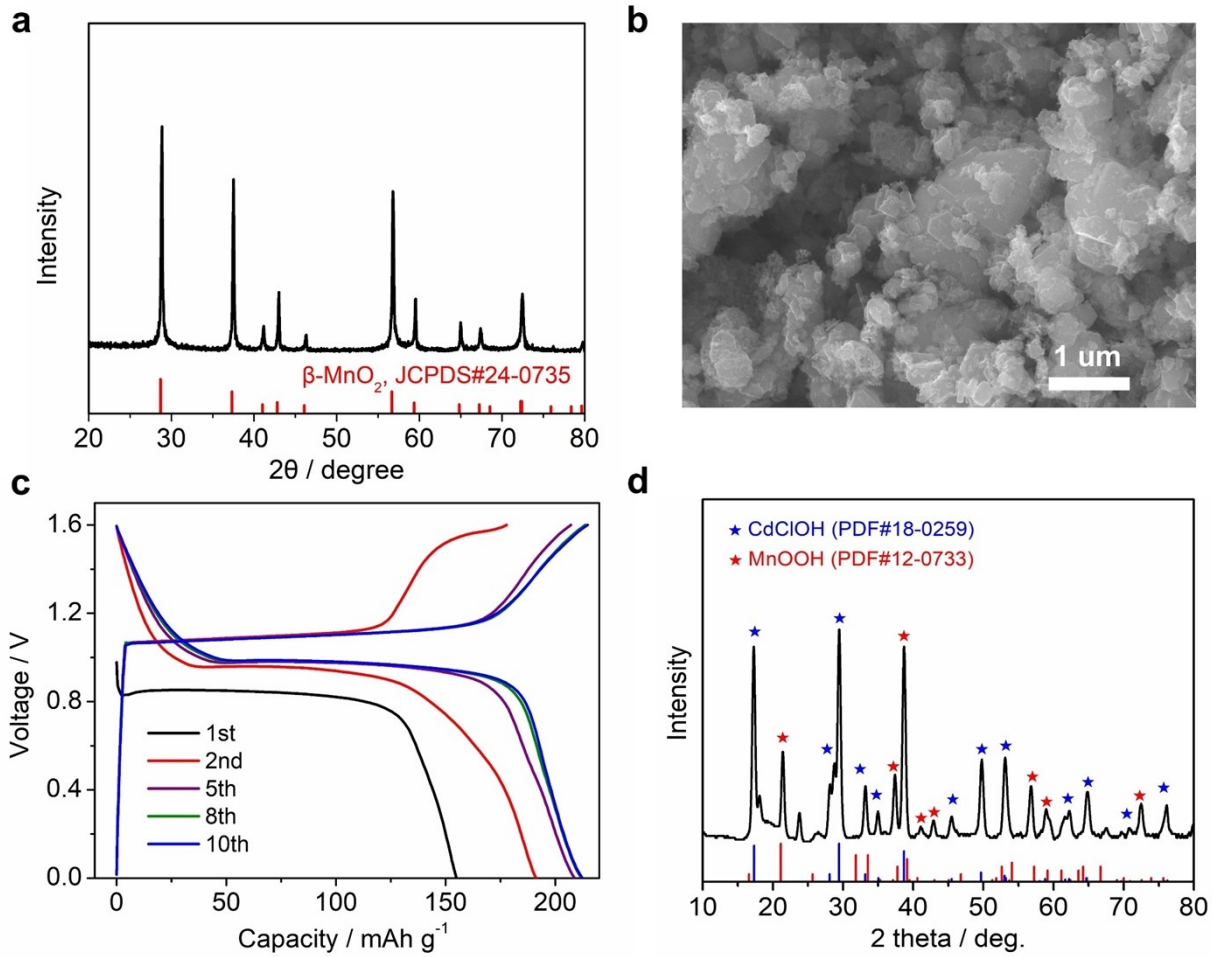

Figure S27. The performance of the micro-sized β-MnO_2 electrode. (a) The XRD pattern; (b) The SEM image; (c) The charge/discharge curves at 100 mA g^{-1}; (d) The XRD pattern of the MnO_2 electrode after the first discharge. The micro-sized β-MnO_2 electrode was commercially avaliable and purchased from HiMedia (>99.0% purity). The self-standing β-MnO_2 electrode was made in a similar way to that of MnO_2 nanorod material. After the first discharge process, the self-standing film was washed by 1 M HCl solution 3 times, and each time lasted 30 seconds. This process can reduce the CdClOH precipitation and expose more MnOOH for XRD detection.

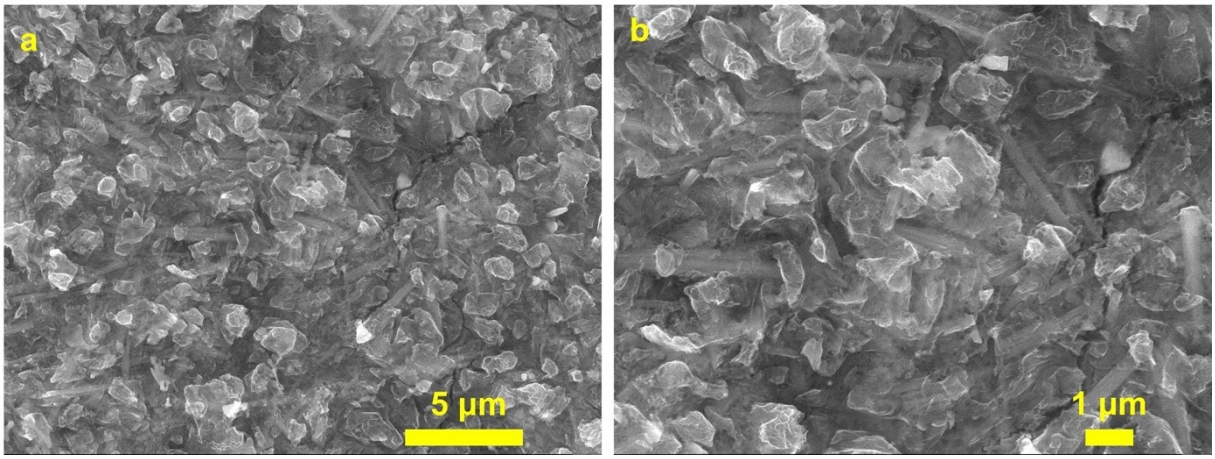

Figure S28. SEM images of the MnO_2 electrode at the charged state (point C).

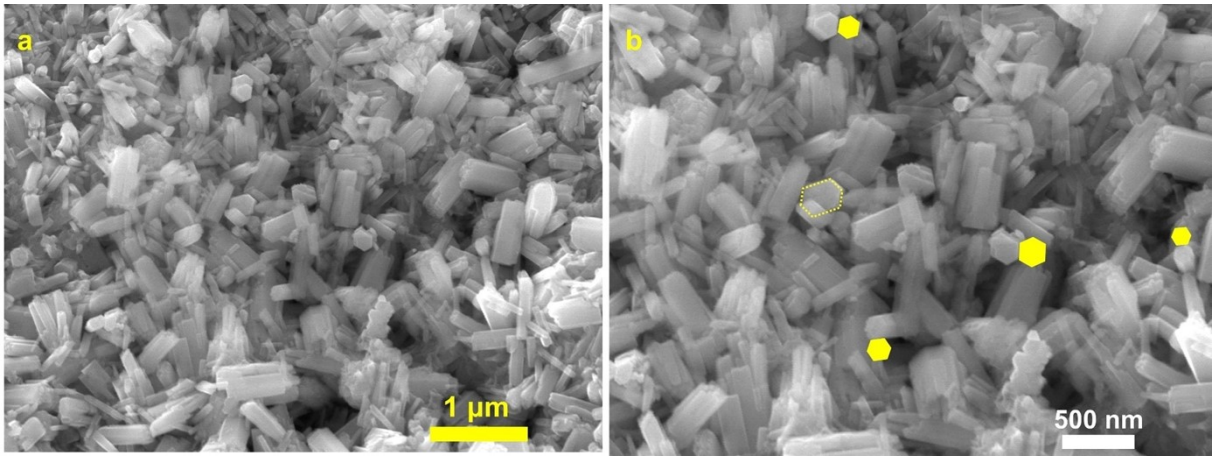

Figure S29. SEM images of the MnO_2 electrode at the second discharge state (point D).

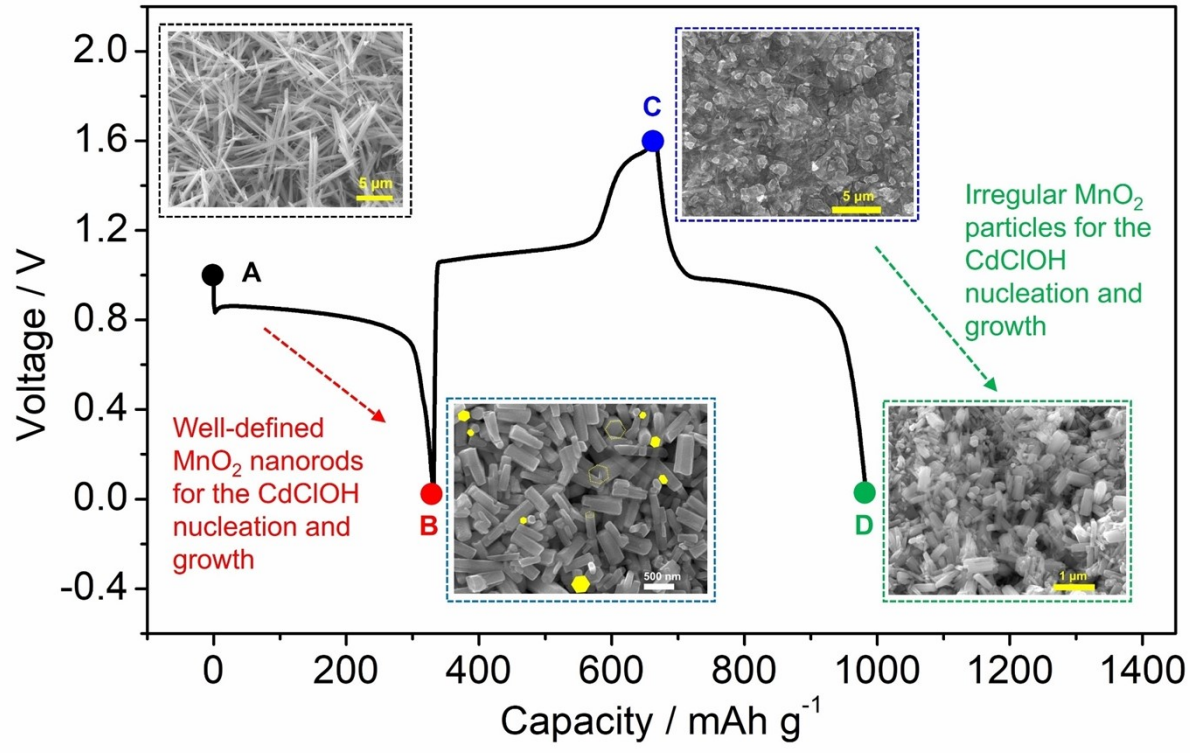

Figure S30. The influence of the MnO_2 material on the CdClOH precipitation morphology. The MnO_2 material provides the nucleation sites for the CdClOH; therefore, the MnO_2 material status will influence the final morphology of the CdClOH precipitation.

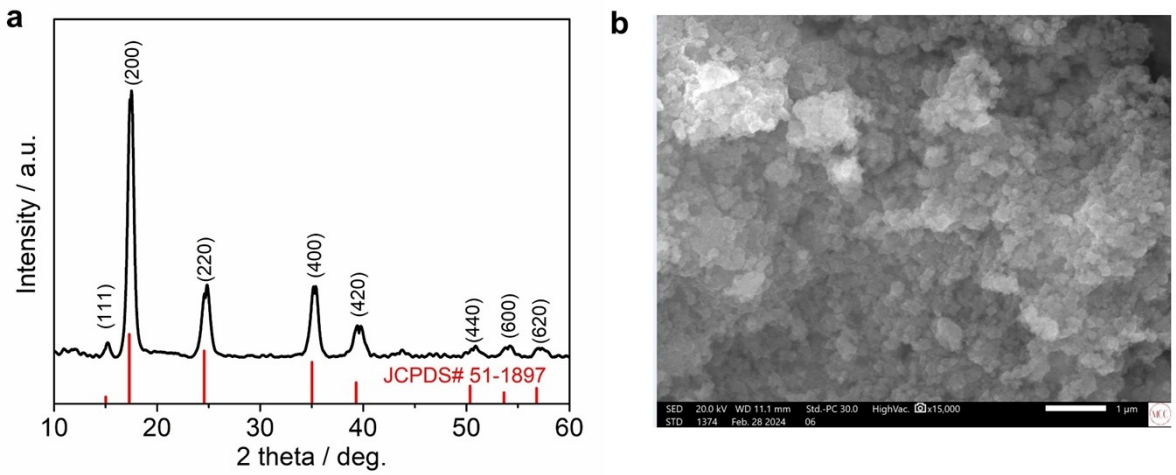

Figure S31. Physical characterization of the $KNiFe(CN)_6$ material. (a) The XRD pattern and the standard PDF card; (b) The SEM image.

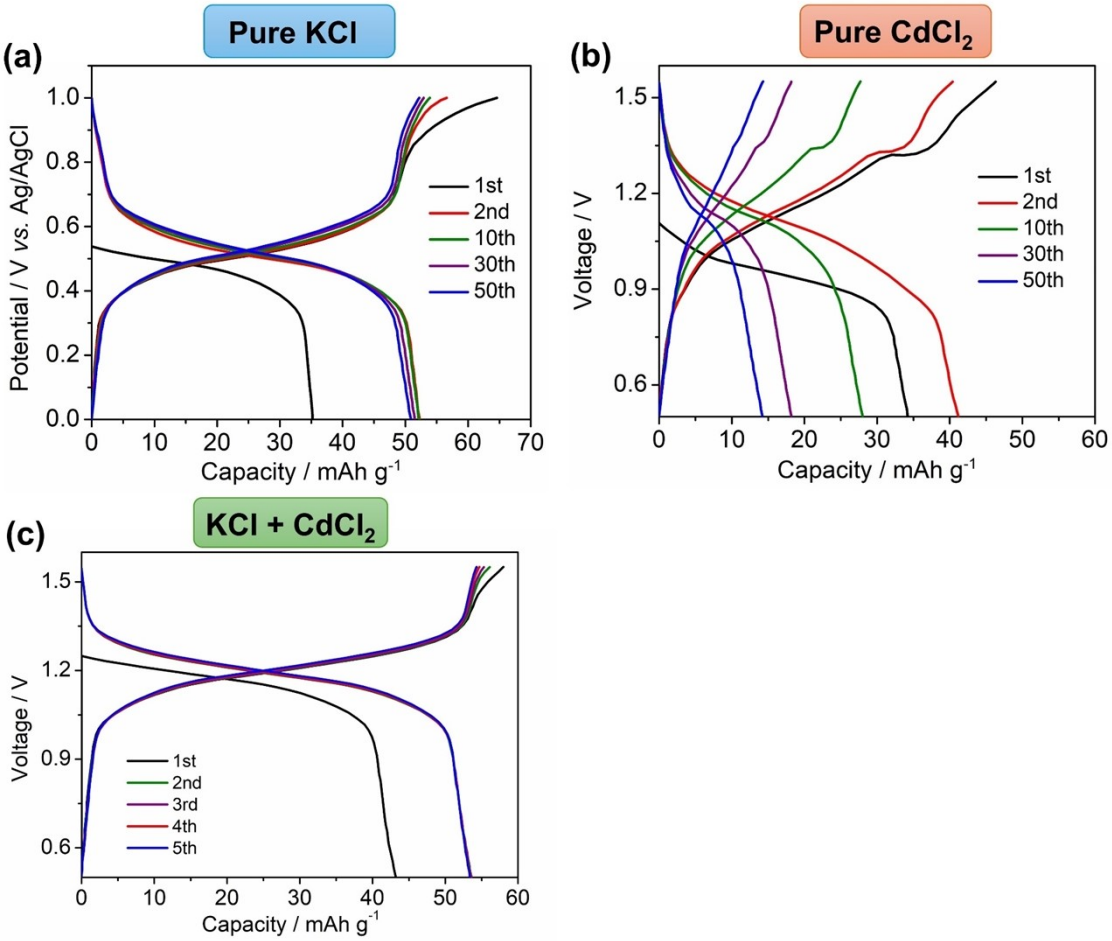

Figure S32. GCD curves of the $KNiFe(CN)_6$ in different electrolytes. (a) The three-electrode AC‖$KNiFe(CN)_6$ battery in the pure 1 M KCl electrolyte, where saturated Ag/AgCl works as the reference electrode; (b) The two-electrode Cd‖$KNiFe(CN)_6$ battery in the pure 1 M $CdCl_2$ electrolyte; (c) The two-electrode Cd‖$KNiFe(CN)_6$ battery in the hybrid $CdCl_2$ + KCl electrolyte.

As shown, the K^+ insertion in the $KNiFe(CN)_6$ cathode is very stable and appears as S-shaped reaction slopes, leading to a discharge capacity of ~52 mAh g^{-1}. This performance is akin to that of Cd‖$KNiFe(CN)_6$ battery in the hybrid $CdCl_2$ + KCl electrolyte, with typical S-shaped reaction slopes and a reversible capacity of ~52 mAh g^{-1}. By contrast, when the Cd‖$KNiFe(CN)_6$ battery is tested in the pure $CdCl_2$ electrolyte, it shows an ill-defined GCD curves, lower reaction capacity, and fast capacity fading. These comparative studies can prove the K^+ insertion into the $KNiFe(CN)_6$ cathode.

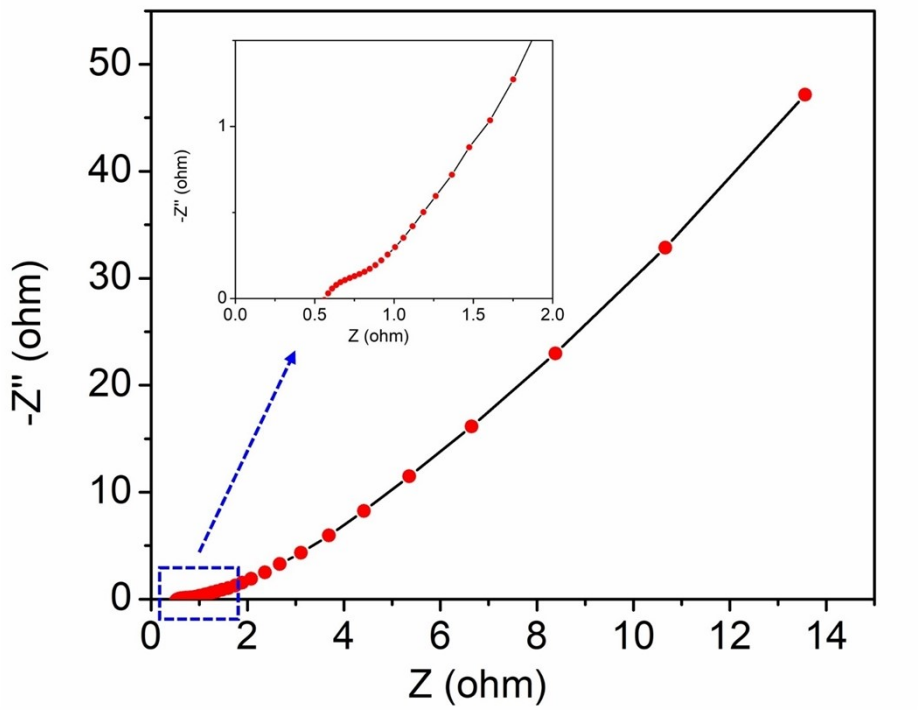

Figure S33. The EIS result of the Cd‖KNiFe(CN)$_6$ battery. There is a suppressed semi-circle plus a linear line, which is attributed to the charge-transfer resistance (R_{ct}) and ion diffusion, respectively. The R_{ct} value is found to be as low as ~0.35 Ω, which facilitates the fast K^+ insertion process in the open KNiFe(CN)$_6$ framework.

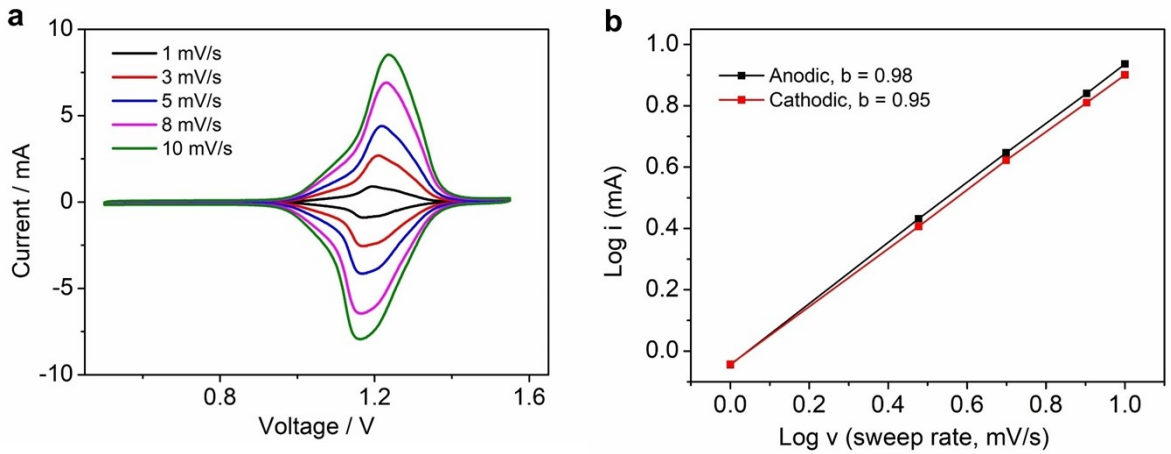

Figure S34. The CV analysis of the Cd‖KNiFe(CN)$_6$ battery. (a) CV curves at different scanning rates; (b) The log relationship between the current and scanning rates. As shown, both the anodic and cathodic peaks have a *b* value of ~1.0, which corresponds to a capactive intercalation process. This accounts for the super-high rate performance of the Cd‖KNiFe(CN)$_6$ battery.

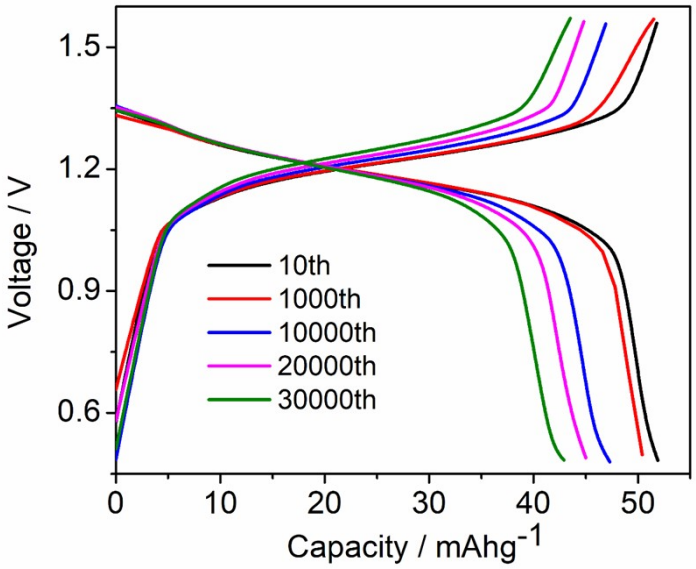

Figure S35. The selected GCD curves of the Cd-KNiFe(CN)$_6$ battery during cycling.

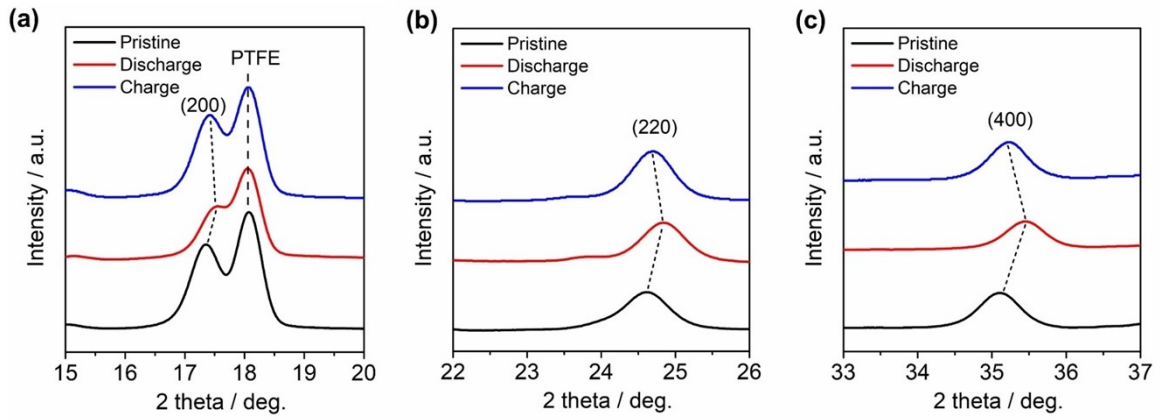

Figure S36. The ex-situ XRD patterns of the $KNiFe(CN)_6$ cathode. (a) The (200) peak; (b) The (220) peak; (c) The (400) peak. As shown, during discharge, the (200), (220), and (400) peaks shifted to a higher diffraction position, suggesting a lattice shrinkage. This is because the ionic radius of $[Fe^{II}(CN)_6]^{4-}$ is smaller than that of $[Fe^{III}(CN)_6]^{3-}$. During charge, these peaks are restored to their original positions, indicating reaction reversibility. The d_{200} lattice changes from 10.22 Å (charged) to 10.12 Å (discharged), leading to a small volume change of 3%, which accounts for the excellent cycling stability.

References

[1] Prices of chemical elements. *Wikipedia*. https://en.wikipedia.org/wiki/Prices_of_chemical_elements (accessed on Jan 17th, 2024).

[2] Fei Wang, *et al.* Highly reversible zinc metal anode for aqueous batteries. ***Nat. Mater.*** 2018, 17(6): 543-549.

[3] Chong Zhang, *et al.* The electrolyte comprising more robust water and superhalides transforms Zn-metal anode reversibly and dendrite-free. ***Carbon Energy***, 2021, 3(2): 339-348.

[4] Heng Jiang, *et al.* Chloride electrolyte enabled practical zinc metal battery with a near-unity Coulombic efficiency. ***Nat. Sustain.***, 2023: 1-10. DOI: 10.1038/s41893-023-01092-x.

[5] Longsheng Cao, *et al.* Fluorinated interphase enables reversible aqueous zinc battery chemistries. ***Nat. Nanotechnol.***, 2021, 16(8): 902-910.

[6] Longsheng Cao, et al. Highly Reversible Aqueous Zinc Batteries Enabled by Zincophilic–Zincophobic Interfacial Layers and Interrupted Hydrogen-Bond Electrolytes. ***Angew. Chem. Int. Ed.*** 2021, 60, 18845-18851.

[7] Ruirui Zhao, *et al.* Lanthanum nitrate as aqueous electrolyte additive for favourable zinc metal electrodeposition. ***Nat. Commun.***, 2022, 13(1): 3252.

[8] Junnan Hao, *et al.* Boosting zinc electrode reversibility in aqueous electrolytes by using low-cost antisolvents. ***Angew. Chem. Int. Ed.***, 2021, 60(13): 7366-7375.

[9] Stefan Ilic, et al. Effect of Antisolvent Additives in Aqueous Zinc Sulfate Electrolytes for Zinc Metal Anodes: The Case of Acetonitrile. ***ACS Energy Lett.*** 2024, 9(1): 201–208.

[10] Xiaoqin Zhang, et al. Efficient Suppression of Dendrites and Side Reactions by Strong Electrostatic Shielding Effect via the Additive of Rb_2SO_4 for Anodes in Aqueous Zinc-Ion Batteries, ***Small***, 2023, 19(52): 2303906.

[11] Aruuhan Bayaguud, *et al.* Cationic Surfactant-Type Electrolyte Additive Enables Three-Dimensional Dendrite-Free Zinc Anode for Stable Zinc-Ion Batteries, ***ACS Energy Lett.*** 2020, 5 (9): 3012-3020.

[12] Shangqing Jiao, *et al.* Ion sieve: tailoring Zn^{2+} desolvation kinetics and flux toward dendrite-free metallic zinc anodes. ***ACS Nano***, 2021, 16(1): 1013-1024.

[13] Xuesong Xie, *et al.* Manipulating the ion-transfer kinetics and interface stability for high-performance zinc metal anodes. ***Energy & Environ. Sci.***, 2020, 13(2): 503-510.

[14] Zhuo Wang, *et al.* A metal-organic framework host for highly reversible dendrite-free zinc metal anodes. ***Joule***, 2019, 3(5): 1289-1300.

[15] Shiying Li, *et al.* Toward planar and dendrite-free Zn electrodepositions by regulating Sn-crystal textured surface. ***Adv. Mater.***, 2021, 33(21): 2008424.

[16] Zhao Cai, *et al.* A replacement reaction enabled interdigitated metal/solid electrolyte architecture for battery cycling at 20 mA cm^{-2} and 20 mAh cm^{-2}. ***J. Am. Chem. Soc.***, 2021, 143(8): 3143-3152.

[17] Chong Bai, *et al.* A high-power aqueous rechargeable Fe-I2 battery. ***Energy Storage Mater.***, 2020, 28: 247-254.

[18] Xianyong Wu, et al. Rechargeable iron–sulfur battery without polysulfide shuttling. ***Adv. Energy Mater.*** 2019, 9: 1902422.

[19] Qi Yang, *et al.* Activating C-coordinated iron of iron hexacyanoferrate for Zn hybrid-ion batteries with 10 000-cycle lifespan and superior rate capability. ***Adv. Mater.***, 2019, 31(32): 1901521.

[20] Leyuan Zhang, *et al.* Towards high-voltage aqueous metal-ion batteries beyond 1.5 V: the zinc/zinc hexacyanoferrate system. ***Adv. Energy Mater.***, 2015, 5(2): 1400930.

[21] Wei Sun, *et al.* Zn/MnO_2 battery chemistry with H^+ and Zn^{2+} coinsertion. ***J. Am. Chem. Soc.***, 2017, 139(29): 9775-9778.

[22] Huilin Pan, *et al.* Reversible aqueous zinc/manganese oxide energy storage from conversion reactions. ***Nat. Energy***, 2016, 1(5): 1-7.

[23] Mengyu Yan, *et al.* Water-lubricated intercalation in $V_2O_5{\cdot}nH_2O$ for high-capacity and high-rate aqueous rechargeable zinc batteries. ***Adv. Mater.***, 2018, 30(1): 1703725.

[24] Dipan Kundu, *et al.* A high-capacity and long-life aqueous rechargeable zinc battery using a metal oxide intercalation cathode. ***Nat. Energy***, 2016, 1(10): 1-8.

[25] Zhaolong Li, *et al.* Mechanistic insight into the electrochemical performance of Zn/VO_2 batteries with an aqueous $ZnSO_4$ electrolyte. ***Adv. Energy Mater.***, 2019, 9(22): 1900237.